学位論文

Adsorption, desorption and thin film growth of water molecules on the Rh(111) surface

Rh(111)表面における水分子の吸着、脱離、そして薄膜成長

紅谷　篤史

Adsorption, desorption and thin film growth of water molecules on the Rh(111) surface

A Thesis Submitted to The University of Tokyo

for the Degree of Doctor of Science

(Hakase (Kagaku))

Atsushi Beniya

December, 2007

Abstract

Water-surface interactions play significant roles for our lives and voluminous studies are reported. Electrochemists postulate the electric double layer at the interface between the solid electrode and an aqueous solution. In order to establish the basic theory of electrochemistry, it is of considerable significance to elucidate the structure of the electric double layer. Numerous heterogeneous catalytic reactions involve water molecules as reactant and product, and water molecules have effects on chemical kinetics in other catalytic reactions. Therefore, it is important to elucidate how water molecules adsorb, behave, and arrange themselves on solid surfaces in order to understand microscopic mechanisms in these phenomena.

In this thesis, the interaction of water molecules with the Rh(111) surface was investigated using several surface science techniques such as infrared reflection absorption spectroscopy. The main topics of the present work are to clarify the following points: (1) transient diffusion and cluster formation of water molecules at 20 K, (2) adsorption and desorption kinetics, and (3) the first water layer and thin film growth.

The initial stage of water adsorption on Rh(111) at 20 K was investigated. In the low coverage region, isolated water molecules and small water clusters are observed. Since thermal diffusion is suppressed at 20 K, the formation of water clusters at low coverage is controlled by both coverage and transient diffusion on the surface. Within a simple isotropic diffusion model as the transient diffusion and clustering process, we estimate the mean lateral displacement from the first impact point to the final adsorption site to be 7.6 Å; an incoming water molecule on Rh(111) is adsorbed with eight post-collision hops on the average.

Adsorption and desorption kinetics of water molecules on the Rh(111) surface were investigated using temperature programed desorption. Water molecules show a coverage dependent sticking probability and initial sticking probability was estimated to be 0.46. In desorption process, water molecules exhibit coexistence of a dilute, gas like phase together with islands of a condensed phase, both being two dimensional. Apparent fractional-order desorption can be interpreted as a first-order desorption from two-phase adsorbate with different sticking probabilities. And then, coverage dependence of activation energy and preexponential factor for desorption were estimated. As a result it is clarified that the first layer is energetically stable compared with the multilayer film, and this is clear evidence of wetting.

The adsorption states and growth process of the first water (D_2O) layer and multilayer on Rh(111) were investigated. At the initial stage, water molecules form the commensurate $(\sqrt{3}\times\sqrt{3})R30^\circ$structure. This is flatter than an ice-like bilayer, and consists of D-down species; the D-down species represent water molecule which have free OD pointing to the substrate. D-down islands may have jagged edges. With increasing coverage, the ice-like bilayer (D-up) grows and shows a incommensurate structure; the D-up species represent water molecule which have free OD pointing to a vacuum. At nearly the saturation coverage, the ice-like bilayer is ~9 % compressed from the commensurate $(\sqrt{3}\times\sqrt{3})R30^\circ$structure, which is ~5% compression with respect to ice I_h. At saturation coverage, the first water layer consists of the ice-like bilayer (D-up) and flat (D-down) domains, where the D-up domains occupy 44 % and the D-down domains occupy 56 % in coverage. Further adsorption of water molecules form ice crystallites that do not wet the first water layer and a second layer starts to grow on the D-down domains where the D-down species do not reorient to accommodate formation of a crystalline ice. This is clear evidence of the hydrophobic first water layer.

Acknowledgements

First of all, I would like to express my deepest gratitude to Professor Jun Yoshinobu. He supervised me during my master and doctor program, and taught the fundament for research in the field of physical chemistry, especially the surface science. His supervisions, encouragements, and supports are invaluable to complete the thesis.

I sincerely say gratitude to Dr. Yoshiyuki Yamashita and Mr. Kozo Mukai for their fruitful discussions and a lot of advises. They also gave me a lot of instructions, encouragements, and supports. I also express my gratitude to Dr. Susumu Yamamoto. I was guided by him during my master program, and was gave a lot of instructions and encouragements. I have interested in the water-metal interaction in the period with him. I would like to thank Professor Yoshitada Morikawa and Dr. Ikutaro Hamada (Osaka University) for their fruitful discussions.

Many thanks go to all the members of Yoshinobu Laboratory, Dr. Masayuki Furuhashi, Mr. Kazuhiro Oguchi, Mr. Tetsuo Katayama, Mr. Yu Okubo, and Mr. Yuji Sakaguchi. I would like to thank the previous members of Yoshinobu laboratory, Dr. Md. Zakir Hossain, Dr. Masashi Nagao, Dr. Youhei Kakehuda, Dr. Noriyuki Tsukahara, Dr. Tetsuya Narushima, Dr. Tomohiro Matsui, Mr. Hirobumi Umeyama, Mr. Yuma Kagata, Mr. Katsumasa Yamasaki, and Ms. Ayako Oomura.

Many thanks go to the colleagues in Surface Science group of The Institute for Solid State Physics (ISSP); Professor Fumio Komori, Professor Yukio Hasegawa; all the members of Komori and Hasegawa Laboratories.

A special thanks goes to the secretaries of Division of Nanoscale Science, Ms. Rie Nakatsuzi, Ms. Junko Kawamura, and Ms. Akiko Ono.

I would like to acknowledge the financial support from the 21st century COE for my employment as a research assistant, and the Japan Student Services Organization for scholarship support.

Last but not least, to my family: grandpa, grandma, papa, mama, naoko, and shinpei.

Atsushi Beniya, Kashiwa, December, 2007

Contents

Chapter 1

Introduction

1.1 General Introduction

Water is the principal constituent for life on earth, and provides us with many scientific questions. One of its widely known anomalies is that liquid water has a high density that increases on heating up to 4 °C. In addition solid water exists in a wider variety of stable (and metastable) crystal and amorphous structures than other materials.[1-3] The phase diagram of ice is shown in Fig. 1.1. Thirteen crystal phases have been identified to date, in which hexagonal ice (I_h) is the most stable phase on earth. Recently, it was elucidated that water molecules exist in space as an amorphous ice, which plays an important role in the molecular evolution of dense cloud in the interstellar medium.[4-6]

The interaction of water with metal surfaces is also a topic of interest and research in wide scientific fields such as electrochemistry, catalytic reactions, solar energy conversion, meteorology, and corrosion chemistry.[7,8] Electrochemists postulate the electric double layer at the interface between the solid electrode and an aqueous solution. The electrical potential between electrodes is mainly formed and a charge transfer reaction proceeds in this layer region. In order to establish the basic theory of electrochemistry, it is of considerable significance to elucidate the structure of the electric double layer, and a developing topic.[9] In addition numerous heterogeneous catalytic reactions involve water molecules as reactants and products (e.g. a water-gas shift reaction), and water molecules have effects on chemical kinetics in other catalytic reactions.[10] In solar energy conversion processes water molecules must dissociate to produce hydrogen molecules. Therefore, in order to design an effective fuel cell, understanding the reaction mechanism of water dissociation on the surface is the key.[7,8] Meteorologists are interested in the mechanism of ice or water nucleation at surfaces, since this mechanism is exploited whenever cloud-seeding is used to bring about precipitation. [7,8]

As described above, water-metal interactions have significant roles in our lives, meaning it is important to elucidate how water molecules behave and arrange themselves on surfaces at a molecular level in order to understand these phenomena and the factors that determine the mechanism of ice or water nucleation. The present thesis aims to understand the microscopic behavior and structure of water on a single metal surface using modern surface science techniques.

1.2 Water molecules on metal surfaces

Many experimental and theoretical studies for interactions between adsorbed water molecules and single crystalline metal surfaces were reported as a prototype system for understanding water-solid interfaces.[7,8] Traditionally, it is experimentally revealed that water interacts weakly with transition metal surfaces[11] and this strength is comparable with water-water interaction (i.e. a hydrogen bond).[7,8] In a decade and a half, the increased capability of surface scientists to probe at a molecular level has resulted in more detailed information concerning the properties of adsorbed water molecules on metal surfaces.[12] However, much controversy and many open questions still remain, e.g. the structure and growth process from the first water layer to multilayer ice. The typical processes of water molecules on metal surfaces are schematically illustrated in Fig. 1.2.

As a water molecule impinges to a surface, it binds weakly to the surface as an isolated water molecule (*monomer*).[8,12] When it collides with the surface, it does not adsorb at the collision point but laterally migrates on the surface. This mobility of molecules prior to adsorption is called *transient surface diffusion*.[13] It is difficult to experimentally observe the transient state because this process is dynamic and the time scale is ~ps. On the other hand, the water molecule, which could not adsorb, is reflected from the surface. It is generally thought that incoming water molecules are rarely reflected from metal surfaces.[7]

The adsorbed water monomer is experimentally observed only at low temperatures.[14-20] The water monomer adsorbs at atop sites (above the substrate atom) and it was shown that the molecular plane is significantly tilted relative to the surface normal. A theoretical calculation predicted that when water lies flat (with the molecular plane nearly parallel to the surface) the $1b_1$ (lone pair) derived orbitals undergo the largest mixing with the surface and experience the greatest stabilization.[21]

With increasing temperature, water molecules start thermally diffusing on the surface and collide with each other, consequently forming hydrogen-bonded water clusters (e.g. dimer, hexamer, and two-dimensional islands). Few experimental studies are reported for water surface diffusion,[22-24] but it is thought that the weak water-metal interactions on metal surfaces facilitate water diffusion.[7]

Among these adsorbed structures the two-dimensional (2D) islands have been intensively investigated.[7,8,12] However, their structure and properties have not been elucidated because they reflect interplay between water-water and water-substrate interactions. [8,12] From an energetic perspective, this interplay can be divided into three categories as follows:[7,8] (1) water-water interactions are stronger than water-surface interactions; meaning water molecules do not wet the surface and form three-dimensional (3D) islands, (2) water-surface interactions are stronger than water-water interactions; hence water molecules wet the surface, and (3) water-surface interactions are much stronger than water-water interactions; hence water molecules dissociate on the surface. In the case of transition metal surfaces, since the water-water and water-surface interaction is of comparable strength, the structure of the water layer may be highly dependent on the surface. [8,12,25-29]

A traditional structural model of the 2D island is based on the basal plane of the ice I_h, thus this model is called an *ice–like bilayer* or *puckered bilayer* (BL, 1 BL = 2/3 ML; monolayer), and shown in Fig. 1.3(a and b). This model was proposed assuming a tetrahedral arrangement of water molecules, which are arranged in buckled hexagonal rings.[30] The ice-like bilayer model, in which half the water molecules bind to the substrate via their oxygen lone pair and the remainder have the free OH dangling into a vacuum, is referred to as the "*H-up*" model.

The low energy electron diffraction (LEED) of the water layer on fcc(111) and hcp(0001) often showed a $(\sqrt{3}\times\sqrt{3})R30°$, meaning the ice-like bilayer was considered to be a general model of the first water layer.[7,8] However, more recent LEED studies of H_2O on Ru(0001) have revealed that all oxygen atoms are virtually co–planar and the bilayer buckling was found to be only 0.10 Å, instead of 0.96 Å in ice I_h [the "*compressed bilayer*" model, Fig. 1.3(c)].[31,32]

Recently, a combined x–ray spectroscopy and computational study has presented a new model, in which the first layer is nearly co-planar on Pt(111) and the free OH bonds in the higher lying water are oriented toward the metal substrate [the "*H-down*" model, Fig. 1.3(d)].[33] In this H-down model, all the molecules bind directly to the surface and to each other through lateral hydrogen bonds: all hydrogen bonds are saturated.

Recently, Feibelman, using density functional theory (DFT) calculations proposed that the virtually co–planar geometry on Ru(0001) could be explained by his "*half–dissociated*" water model [Fig. 1.3(e)],[34] where water molecules and hydroxyl fragments are hydrogen–bonded in a hexagonal structure and hydrogen atoms bind directly to the metal. In addition, this model showed a lower total energy with respect to the nondissociative H-up and H-down models.

Besides the controversy in the bilayer, much less is known about the morphology of nanometer scale water films (e.g. coverages greater than 1 BL). The influence of the first water layer on the growth morphology of ice films has recently been demonstrated on Pt(111), where the H-down (i.e. fully coordinated) configuration of the first water layer results in a hydrophobic surface and water molecules form nonwetting 3D ice crystallite on the first water layer as shown in Fig. 1.2.[35,36] Thus, water ice films grow a Stranski-Krastanov mechanism (2D layer + 3D islands) on the Pt(111) surface. The same growth mechanism was also observed on Pd(111)[36] and Ru(0001)[37,38]. Based on the above idea, the H-up configuration may result in a hydrophilic surface, although this is unclear.

At a higher temperature, sufficient to break the intermolecular hydrogen bond, a water molecule escapes from the islands into the bare substrate and finally desorbs from the surface. The desorption kinetics involved is very informative in understanding the equilibrium and the rate process on the surface, although the analysis of desorption kinetics sometimes becomes difficult because desorption may consist of many elementary steps (e.g. detachment from the island and terrace diffusion). Therefore, in contrast to the number of reports on the water desorption, the volume of quantitative studies for desorption kinetics is limited.[7]

1.3 The aim of this thesis

In this study, I chose the Rh(111) surface as an underlying substrate in order to elucidate the microscopic behavior and adsorption structure of water molecules. The Rh(111) surface is one of the few substrates where the lattice mismatch with the basal plane of ice I_h is very small, and the adsorption energy of water may be relatively large, as shown in Fig. 1.4, meaning it would be a good template to study the water ice growth, although it has been studied relatively little compared to other substrates, such as Pt(111) and Ru(0001).[40-44] One of the goals in this study is to gain a general understanding of how the underlying metal substrate influences the wetting ability of the water ice, by comparing the present results on Rh(111) with previous results on other metal surfaces.

In contrast to the number of studies for water-metal systems, consistent results have not been obtained. This is because, in much previous literature, the adsorbed water on metal surfaces may have been affected by x-ray and/or electron induced modification,[45-47] meaning non- or less destructive experimental methods are crucial. With this in mind, I used the following experimental techniques: infrared reflection adsorption spectroscopy (IRAS), spot-profile-analysis low energy electron diffraction (SPA-LEED), and temperature programed desorption (TPD). In addition, the surface impurities and defects were carefully controlled. Under these conditions, I investigated the following topics.

(1) Transient surface diffusion during the water adsorption process

The transient diffusion of adsorbates is difficult to observe experimentally. In this thesis, I estimate the transient diffusion length by measuring the coverage dependence of an adsorbed water monomer at a low temperature and using a simple isotropic diffusion model. Subsequently, I estimated the mean lateral displacement from the first impact point to the final adsorption site to be 7.6 Å.

(2) Adsorption and desorption kinetics

Adsorption is the first step in the surface processes of adsorbates, and desorption kinetics provide the strength of adsorbate-substrate interaction. Thus many experimental studies are reported for adsorption/desorption kinetics of water molecules, although controversies still exist: namely, the reaction order and kinetic parameters. In this thesis, the adsorption and desorption kinetics of water molecules on the Rh(111) surface are investigated, allowing a consistent picture of adsorption and desorption kinetics to be obtained, and the coverage dependence of activation energy and preexponential factor to be estimated. Consequently, I elucidated that water molecules in the first layer are energetically stable compared to the multilayer, hence wetting occurs.

(3) Structure of the first water layer and the multilayer growth process

The microscopic structure of the first water layer continues to be a subject of great interest. In this thesis, the adsorption states and growth process of the first water layer and multilayer on Rh(111) are investigated. Then water molecules show a coverage dependent structures in the first layer and it is elucidated that these structures significantly affect the growth mechanism of multilayer ice.

Figures

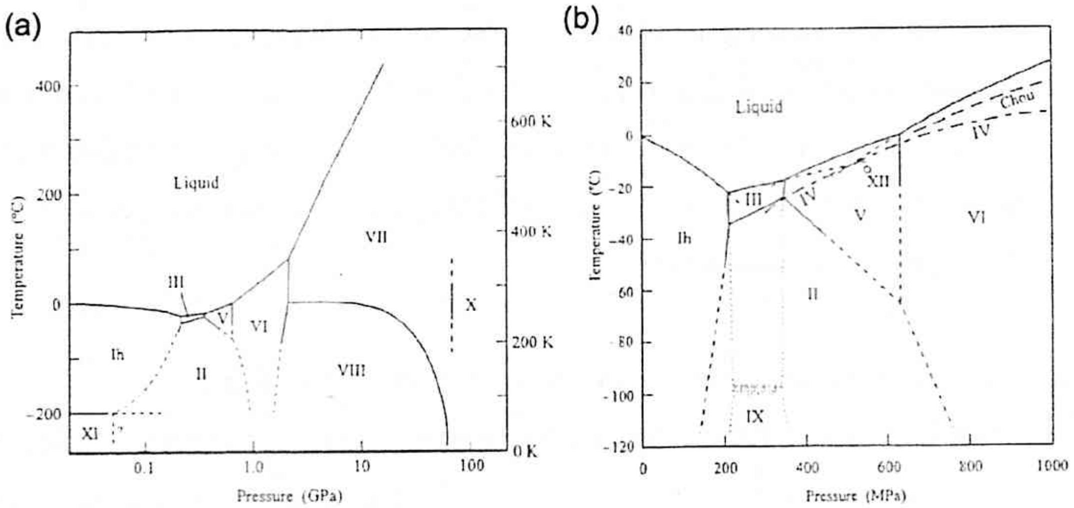

Fig. 1. 1. (a) The phase diagram of ice. (b) Magnified view of the figure (a).[3]

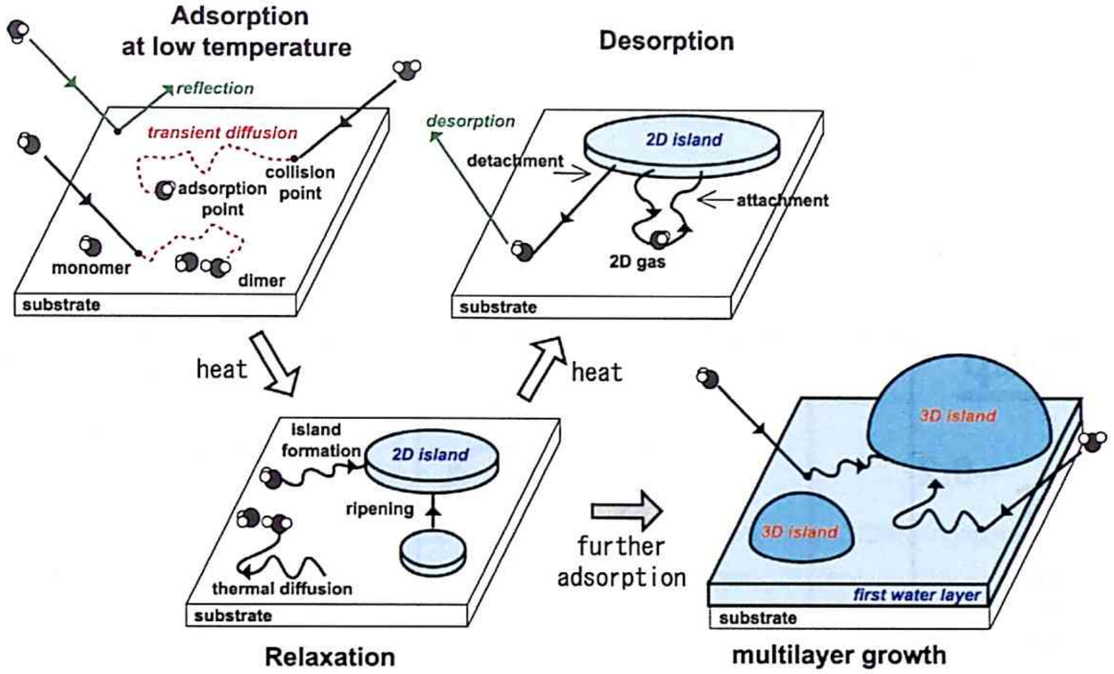

Fig. 1. 2. A schematic of surface processes of water molecules.

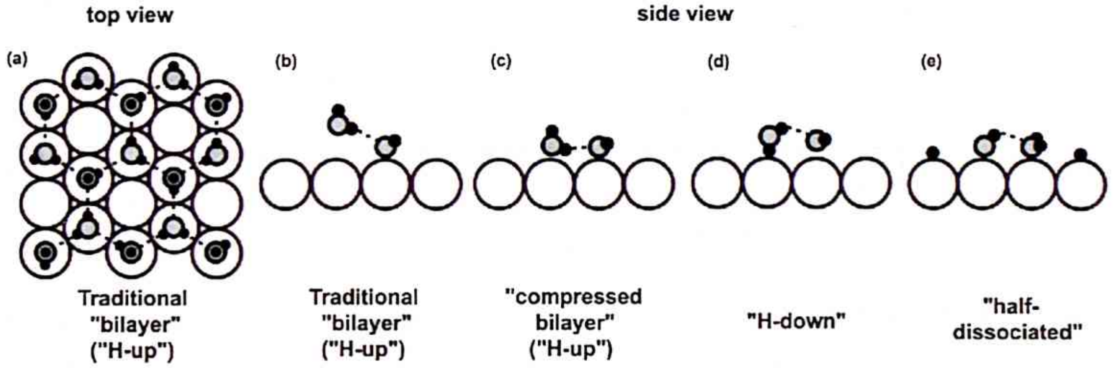

Fig. 1. 3. Various proposed models of the first water layer on transition metal surfaces. (a) Top view of an ice–like "bilayer" model and (b-e) side view of various structural models. Large, middle, and small circles represent metal atoms, O atoms, and H atoms, respectively. Dashed line represents a hydrogen bond. (b) Side view of an ice–like "bilayer" model derived from bulk ice I_h. (c) Side view of a "compressed bilayer" model. (d) Side view of a "H-down" model. (e) Side view of a "half–dissociated" model.

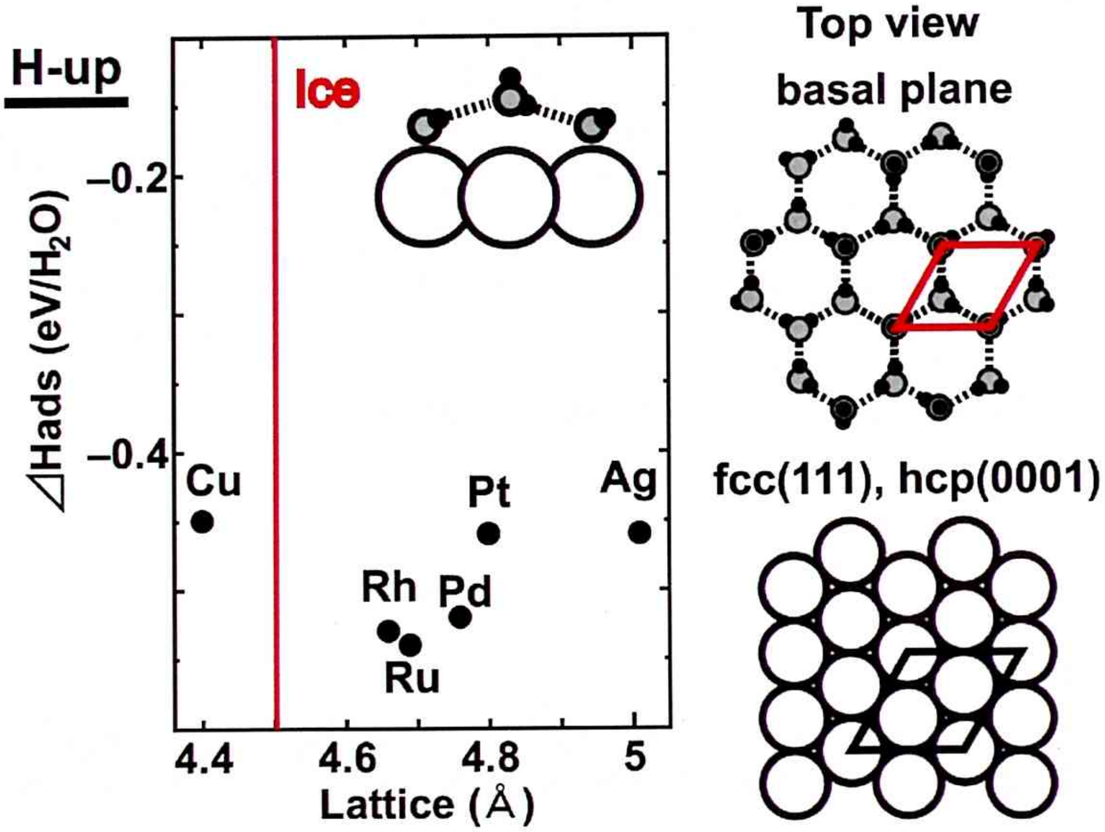

Fig. 1. 4. Calculated adsorption enthalpy of water adlayer with H-up model on various close-packed metal surfaces[39]. Lattice is represented in √3a, where a is the lattice constant of the metal surface. Vertical red line is the lattice constant of the I_h basal plane, 4.52 Å.

References

1. D. Eisenberg and W. Kauzmann, *The Structure and Properties of Water* (Oxford University Press, New York, 1969).
2. C. A. Angell, Annu. Rev. Phys. Chem. **55**, 559 (2004).
3. V.F.Petrenko, R.W.Whitworth, *Physics of Ice* (Oxford University Press, New York,1999)
4. J. M. Greenberg, Surf. Sci. **500**, 793 (2002).
5. D.A Williams and E. Herbst, Surf. Sci. **500**, 823 (2002).
6. T. E. Madey, R. E. Johnson, and T. M. Orlando, Surf. Sci. **500**, 838 (2002).
7. A. Thiel and T. E. Madey, Surf. Sci. Rep. **7**, 211 (1987).
8. M. A. Henderson, Surf. Sci. Rep. **46**, 1 (2002).
9. H. Tamura and Y. Matsuda, *Gendaidenkikagaku* (Baihuukann, Tokyo, 1998) in japanese.
10. R. I. Masel, *Chemical Kinetics and Catalysis* (Wiley, New York, 2001).
11. R. I. Masel, *Principles of adsorption and reaction on solid surfaces* (Wiley, New York, 1996).
12. A. Verdaguer, G. M. Sacha, H. Bluhm, and M. Salmeron: Chem. Rev. **106**, 1478 (2006).
13. J. V. Barth, Surf. Sci. Rep. **40**, 75 (2000).
14. S. Andersson, C. Nyberg and C. G. Tengstål, Chem. Phys. Lett. **104**, 305 (1984).
15. M. Nakamura and M. Ito, Chem. Phys. Lett. **325**, 293 (2000).
16. M. Nakamura and M. Ito, Chem. Phys. Lett. **335**, 170 (2001).
17. M. Nakamura and M. Ito, Chem. Phys. Lett. **384**, 256 (2004).
18. S. Yamamoto, A. Beniya, K. Mukai, Y. Yamashita, and J. Yoshinobu, J. Phys. Chem. B. **109**, 5816 (2005).
19. A. L. Glebov, A. P. Graham, and A. Menzal, Surf. Sci. **427-428**, 22 (1999).
20. H. Ogasawara, J. Yoshinobu, and M. Kawai, J. Chem. Phys. **111**, 7003 (1999).
21. A. Michaelides, V. A. Ranea, P. L. de Andres, and D. A. King, Phys. Rev. Lett. **90**, 216102 (2003).
22. T. Mitsui, M. K. Rose, E. Fomin, D. F. Ogletree, and M. Salmeron, Science. **297**, 1850 (2002).
23. Y. Lilach, V. Buch, and M. Asscher, J. Chem. Phys. **119**, 11899 (2003).
24. E. Fomin, M. Tatarkhanov, T. Mitsui, M. Rose, D. F. Ogletree, and M. Salmeron, Surf. Sci. **600**, 542 (2006).
25. H. Ogasawara, B. Brena, D. Nordlund, M. Nyberg, A. Pelmenschikov, L. G. M. Pettersson, and A. Nilsson, Phys. Rev. Lett. **89**, 276102 (2002).
26. G. Zimbitas, S. Haq, and A. Hodgson, J. Chem. Phys. **123**, 174701 (2005).
27. J. Cerdá, A. Michaelides, M. –L. Bocquet, P. J. Feiblman, T. Mitsui, M. Rose, E. Fomin, and

M. Salmeron, Phys. Rev. Lett. **93**, 116101 (2004).

28. K. Andersson, A. Nikitin, L. G. M. Pettersson, A. Nilsson, and H. Ogasawara, Phys. Rev. Lett. **93**, 196101 (2004).
29. S. Haq, C. Clay, G. R. Darling, G. Zimbitas, and A. Hodgson, Phys. Rev. B. **73**, 115414 (2006).
30. D. L. Doering and T. E. Madey, Surf. Sci. **123**, 305 (1982).
31. G. Held and D. Menzel, Surf. Sci. **316**, 92 (1994).
32. S. R. Puisto, T. J. Lerotholi, G. Held, and D. Menzel, Surf. Rev. Lett. **10**, 487 (2003).
33. H. Ogasawara, B. Brena, D. Nordlund, M. Nyberg, A. Pelmenschikov, L. G. M. Pettersson, and A. Nilsson, Phys. Rev. Lett. **89**, 276102 (2002).
34. P. J. Feibelman, Science. **295**, 99 (2002).
35. G. A. Kimmel, N. G. Petric, Z. Dohnálek, and B. D. Kay, Phys. Rev. Lett. **95**, 166102 (2005).
36. G. A. Kimmel, N. G. Petric, Z. Dohnálek, and B. D. Kay, J. Chem. Phys. **126**, 114702 (2007).
37. S. Haq ans A. Hodgson, J. Phys. Chem. C. **111**, 5946 (2007).
38. T. Kondo, H.S. Kato, M. Bonn, and M. Kawai, J. Chem. Phy. **126**, 181103 (2007).
39. A. Michaelides, Appl. Phys. A. **85**, 415 (2006).
40. J. J. Zinck and W. H. Weinberg, J. Vac. Sci. Technol. **17**, 188 (1980).
41. J. Kiss and F. Solymosi, Surf. Sci. **177**, 191 (1986).
42. F. T. Wagner and T. E. Moylan, Surf. Sci. **191**, 121 (1987).
43. K. D. Gibson, M. Viste, and S. J. Sibener, J. Chem. Phys. **112**, 9582 (2000).
44. S. Yamamoto, A. Beniya, K. Mukai, Y. Yamashita, and J. Yoshinobu, J. Phys. Chem. B. **109**, 5816 (2005).
45. K. Andersson, A. Nikitin, L. G. M. Pettersson, A. Nilsson, and H. Ogasawara, Phys. Rev. Lett. **93**, 196101 (2004).
46. N. S. Faradzhev, K. L. Kostov, P. Feulner, T. E. Madey, and D. Menzel, Chem. Phys. Lett. **415**, 165 (2005).
47. K. Andersson, A. Gómez, C. Glover, D. Nordlund, H. Öström, T. Schiros, O. Takahashi, H. Ogasawara, L. G. M. Pettersson, and A. Nilsson, Surf. Sci. **585**, L183 (2005).

Chapter 2

Fundamental knowledge

In this chapter, a brief summary of the fundamental properties of water and the physical concepts of adsorbate on the surface are presented.

2.1 Water molecules and ice

2.1.1 The isolated water molecule

Water molecules consists of two hydrogen atoms attached to an oxygen atom. The chemical bonding in the isolated molecule is often thought of in terms of a simple Lewis structure, where an oxygen atom contributes six valence electrons and each hydrogen contributes one (Fig. 2.1). The four valence electrons associated solely with the oxygen atom represent two lone pairs, while the four valence electrons shared by the hydrogen and oxygen atoms represent the intramolecular bonds. The two lone pairs enable the oxygen to coordinate to other molecules by acting as an electron donor.

The binding in H_2O results from the interaction of electrons in the $2s^2$ and $2p^4$ atomic orbitals of oxygen with electrons in the $1s^1$ atomic orbitals of the hydrogen atoms. The linear combinations of the atomic orbitals (LCAOs), which make the most significant contribution to the respective molecular orbitals (MOs) of water, are listed in table 2.1. Figure 2.2 shows the five occupied and lowest three unoccupied MOs of an isolated water molecule calculated using the Restricted Hartree-Fock wave function with the 6-31G basis set.[1] The two lowest energy orbitals $1a_1$ and $2a_1$ are contributed from the 1s and 2s (mostly) orbitals of the oxygen atom, respectively, and are consequentially approximately spherical. The three highest energy occupied orbitals ($1b_2$, $3a_1$, $1b_1$) are orthogonal around the oxygen atom and without obvious sp^3 hybridization characteristics. The highest occupied molecular orbital (HOMO), $1b_1$, is predominantly p_y^2 in character with no contribution from the hydrogen 1s orbital and mainly contributes to the lone pair. The $2a_1$, $1b_2$ and $3a_1$ all contribute to the OH bonds. The two lowest unoccupied molecular orbitals $4a_1$ (LUMO) and $2b_2$ are OH antiboding orbitals. The experimental binding energy of the $1a_1$ orbital in the gas phase is 539.9 eV.[2]

These canonical orbitals can also be recast in terms of localized orbitals,[3] which provides a simpler picture, leading to the common model of water in which two equivalent MOs exist for the OH bonds and two exist for the lone pairs, according to the known symmetry of the molecule. In water, two equivalent localized orbitals can be formed along the OH bonds by taking a linear combination of the $1b_2$, $2a_1$ and $3a_1$ MOs, while the nonbonding orbitals forming the lone pairs are contributed from the $1b_1$, $3a_1$ and $2a_1$ orbitals. The orbital transformation leaves the total energy and density invariant, but the localized orbitals are no longer eigenfunctions of the Hartree-Fock Hamiltonian. The usual picture of bonding in the water molecule, in terms of such localized MO's, is shown in Fig. 2.3 and the resultant shape of the molecule is described by four doubly-occupied orbitals arranged quasi-tetrahedrally around the oxygen atom.

2.1.2 The hydrogen bond

The hydrogen bond plays an important role in chemistry and biology, and gives rise to the many unique properties of the most important substance on earth, namely water. A hydrogen bond lies in an energy range intermediate between van der Waals interactions and covalent bonds and is said to exist when:[4]

(1) There is evidence of a local bond.
(2) There is evidence that this bond sterically involves a hydrogen atom already bonded to another atom.

Hydrogen bonds covers a wide and continuous energy scale, ranging from around 2 to nearly 170 kJ/mol.[4] The main components of the hydrogen bond are electrostatic forces, charge transfer, covalent forces, dispersion forces, and exchange repulsion[4], meaning it becomes difficult to apply a rigorous definition for the hydrogen bond, but it can be classified into three different categories depending on energetics and interactions.

(1) Weak: bond energy below 20 kJ/mol mostly arising from van der Waals interaction
(2) Intermediate: bond energy within the range 20-60 kJ/mol mostly arising from electrostatic interaction ($X^{\delta-}$–$H^{\delta+}\cdots A^{\delta-}$)
(3) Strong: bond energy above 60 kJ/mol with a covalent character

The strength of the hydrogen bond in ice and water is generally estimated at 15-25 kJ/mol,[5] which is classified into the weak or intermediate type. Thus we infer that the hydrogen bond between water molecules is derived from mainly van der Waals and electrostatic interaction, but there may be some charge rearrangement upon the formation of hydrogen bonds in order to minimize

Pauli-repulsion and facilitate more favorable electrostatic interaction.[6]

The MOs of the isolated water are appreciably changed by the hydrogen bond. The simplest case is a water dimer $(H_2O)_2$, in which a water molecule acts as a proton donor and the other acts as a proton acceptor. The calculated MOs of isolated water dimer and their eigenvalues are shown in Fig. 2.4. The $1b_2$ and $3a_1$ orbitals are largely responsible for the donation of a hydrogen bond with the $3a_1$ orbital shown experimentally to contribute the most. As a result of the hydrogen bond, the potential energy surface for the H participating in the bond become flatter; the OH bond weakens.[7]

2.1.3 The ice *I*

Each water molecule can form two hydrogen bonds involving their hydrogen atoms plus two further hydrogen bonds utilizing the hydrogen atoms attached to neighboring water molecules. These four hydrogen bonds optimally arrange themselves tetrahedrally around each water molecule, as shown in Fig. 2.5. In ice, this tetrahedral clustering is extensive, producing its crystalline form.[1]

The most common crystalline forms of ice, hexagonal ice I_h and cubic ice I_c, have an oxygen atom situated at the C_{3V} and T_d site of symmetry, respectively.[5] Figure 2.6 shows the positions of the oxygen atoms in ice I_h. Hydrogen atoms are randomly positioned between the oxygen atoms, hence ice *I* has a residual entropy. Hexagonal ice crystals form hexagonal plates and columns, where the top and bottom faces are basal planes by the chair structure, and the side faces are called prism faces due to the boat structure. The basal plane, which consists of upper and lower layers, is often referred to as being "*puckered bilayer*".

2.2 Surface processes of adsorbate

2.1.1 Adsorption and desorption kinetics

A surface posses *surface free energy* which is equal to the work to create a surface from the infinite solid via a cleavage process. The surface free energy per unit area is called *surface tension*. When gas molecules adsorb on a surface, the system entropy decreases because of the loss of freedom (from three- to two-dimensions). Thus, in the adsorption equilibrium condition ($\Delta H = T\Delta S$), the adsorption is an exothermic process. The heat of an adsorption process is called the *adsorption energy*, or *binding energy*. Adsorption is roughly classified into two categories based on the electronic theory: *physisorption* and *chemisorption*. Typical chemisorption energies are 60-400 kJ/mol for simple molecules, which compares to 8-40 kJ/mol for physisorption. When a molecule is chemisorbed, the electrons are shared between the adsorbate and surface, meaning the adsorbate's electronic structure is significantly perturbed, while the surface's electronic structure is perturbed to a lesser extent. In contrast, physisorption is governed by dispersion (i.e. van der Waals) forces. The surface does not share electrons with the adsorbate, meaning the electronic structure of the adsorbate is perturbed to a much lesser extent. Therefore, a more direct test of whether a molecule is physisorbed or chemisorbed is as follows:

- A molecule is *physisorbed* when it adsorbs without undergoing a *significant* change in electronic structure.
- A molecule is *chemisorbed* when the molecule's electronic structure is *significantly* perturbed upon adsorption.

Adsorption kinetics[8,9]

When an incoming molecule collides with a surface it could be *scattered* elastically or inelastically by the surface, where it will remain if it loses enough of its translational energy due to inelastic scattering. In such cases, we say that the molecule is *trapped*. Note, however, that when a molecule is first trapped it has lost sufficient energy to prevent it from immediately leaving the surface. Nevertheless, the molecule is still in a weakly bound mobile state (*precursor*) and while in such state, the thermal motion of the surface atoms can cause the molecule to desorb. Consequently, the molecule should be converted to a more strongly bound state if the molecule stays on the surface for some considerable time. When a molecule collides with a surface, loses its energy, and is converted into a state where the molecule remains on the surface for a reasonable time, we say that the molecule *sticks*. These processes are schematically illustrated in Fig. 2.7. Fundamentally, trapping and sticking processes are quite different. The trapping rates are determined by the rate at which energy is transferred between the incoming molecule and the surface, while sticking rates are determined by the rate at which incoming molecule find sites where they can physisorb or chemisorb.

There are two different kinds of precursor states, i.e. the precursor state over an unoccupied surface sites (*intrinsic precursor*) and that over a site occupied by a chemisorbed species (*extrinsic precursor*). A precursor state does not mean a physisorbed state. When a molecule dissociatively adsorbs, the precursor state is a molecular chemisorption and/or physisorption state.

The rate of adsorption is conventionally expressed as the *sticking probability* or *sticking coefficient*, *S*, defined by:

$$S = \frac{\text{rate of adsorption of moleules by the surface}}{\text{rate of collision of molecules with the surface } (Z)}$$

$$Z = \frac{p}{(2\pi mkT)^{1/2}} \text{cm}^{-2}\text{s}^{-1} \tag{2.1}$$

The sticking probability is unambiguously the probability that an incident molecule is finally adsorbed on the surface with the infinite lifetime of the adsorbed molecule. The probability of an incident molecule trapping into a weakly bound, short-lived state is referred as to the *trapping probability.* At the limit of zero coverage, the sticking probability is known as the *initial sticking probability* S_0, which is dependent on the surface or gas temperature in some cases. If the adsorption is a non-activated process, as depicted in Fig. 2.8(a), S_0 decreases with increasing surface temperature and with increasing gas temperature, while if the adsorption is an activated process, Fig. 2.8(b), S_0 is found to increase with increasing surface and gas temperature.

If there is no adsorption into the bulk, and no formation of a second layer, the sticking probability will eventually fall to zero at saturation coverage due simply to site-blocking. Various types of variation of S with coverage have been observed, which can be divided into six categories as shown in Fig. 2.9. These behaviors are an important indicator of the adsorption mechanism.

(a) This is the simplest case. S shows a linear drop with increasing coverage. If another adsorbate molecule comes in and hits the filled sites, the new adsorbate molecule cannot stick; and instead desorbs. Langmuir showed that if the adsorbate only needs a single site to adsorb, and there are no adsorbate-adsorbate interactions or weakly bound states, then the system show this type of behavior.

(b) The decrease of S is not linear with increasing coverage. The curvature in the S plot can arise for several different reasons. For instance, if the adsorbate dissociatively adsorbs so it blocks two or more sites, this type of behavior will become apparent.

(c) This occurs when the S is nearly constant up to some intermediate coverage, before dropping at higher coverages. This behavior arises because the incoming molecules are initially trapped into a weakly bound *precursor* state, before then moving around the surface and finding a site to adsorb.

(d) In this type, the *S* initially drops with increasing coverage, although beginning to rise at some intermediate coverage. This behavior is often observed in a system showing surface reconstruction.

(e) The *S* initially rises as gas is adsorbed, before subsequently dropping as one fills up sites. Experimentally, this type of behavior occurs mainly in trapping-mediated systems and others where energy transfer plays an important role. Trapping rates increase in the presence of an adsorbate because adsorbate-adsorbate energy transfer is much more efficient than adsorbate-surface energy transfer. Consequently, the *S* initially rises as adsorbate accumulates.

(f) The *S* shows a pattern of plateaus and dips, which is more unusual. In principle, this type can arise if there are multiple adsorption sites or if there is a surface phase transition during the adsorption process.

Statistical thermodynamics of adsorption and desorption[8-11]

The rates of adsorption and desorption processes on surfaces may be conceptualized within the framework of the Eyring theory of reaction rates. This theory postulates that the reaction (adsorption and desorption) proceeds via an energetically activated state (or complex) that is intermediate in structure between the reactants and products in the process under consideration. It exists at the top of a potential energy barrier whose height is the activation energy for the reaction process. Passage over the energy barrier occurs by motion along a path called the reaction coordinate that describes the molecular configuration of the reactants and products. It is proposed that the activated complex at the top of the barrier exists in a low concentration and in equilibrium with the reactants, permitting one to apply statistical theory to the problem.

For adsorption on a uniform surface, let N^* be the equilibrium concentration of activated complexes (molecules cm^{-2}), N_s the number of adsorption sites per cm^2, and N_g the number of gas-phase molecules per cm^3. For an adsorption process in which a molecule is adsorbed without dissociation on a surface, one may write an equilibrium constant involving the reactants and activated complex as:

$$K^*(\mathrm{eq}) = N^*/N_g N_s = f^{*}/f_g f_s \, , \tag{2.2}$$

where the three f terms are the complete partition function for the species or the sites, namely $f = \sum_i g_i \exp(-\varepsilon_i/kT)$ with g_i being the degeneracy of the quantum state energy ε_i. Thus,

$$N^* = f^{*} N_g N_s / f_g f_s \, . \tag{2.3}$$

The rate of the adsorption is equal to the concentration of activated complexes N^* multiplied by the frequency of crossing of the barrier. Let us assume that the activated complex exists in a region of length δ along the reaction coordinate at the top of the barrier. For translation over the barrier the average velocity $\bar{v}$, determined from Maxwell-Boltzmann statistics for a one-dimensional problem, is

$$\bar{v} = \left(kT/2\pi m^*\right)^{1/2} , \tag{2.4}$$

where m^* is the effective mass of the complex and k is the Boltzmann constant. The average time τ of crossing the barrier is

$$\tau = \delta/\bar{v} = \delta\left(2\pi m^*/kT\right)^{1/2} . \tag{2.5}$$

Therefore it follows that the rate of transmission over the barrier is

$$\kappa N^*/\tau \tag{2.6}$$

where κ is a transmission coefficient reflecting the probability that the activated complex will pass over the potential barrier to the product. Thus,

$$-\frac{dN_g}{dt} = \kappa N^*/\tau = \kappa/\tau\left(f^{*'} N_g N_s / f_g f_s\right). \qquad (2.7)$$

Now it is convenient to re-express $f^{*'}$, a complete partition function, as $f^{*'} = f^* f^*_{\text{trans,(1-dim)}}$ where f^* now has removed from it the one-dimensional translational partition function corresponding to motion along the reaction coordinate, over the barrier. From the quantum mechanical considerations of a particle in a one-dimensional box of length δ,

$$f^*_{\text{trans,(1-dim)}} = \left(2\pi m^* kT\right)^{1/2} \delta / h, \qquad (2.8)$$

where h is the plank constant. Therefore, rewriting equation (1.7), we obtain

$$-\frac{dN_g}{dt} = \kappa \frac{kT}{h} \frac{f^*}{f_g f_s} N_g N_s \qquad (2.9)$$

It is convenient to extract from partition function f^* the zero-point energy of the initial state of the system by making this energy the arbitrary zero reference energy, and redefining f* on this basis. This,

$$-\frac{dN_g}{dt} = \kappa \frac{kT}{h} \frac{f^*}{f_g f_s} N_g N_s \exp\left(-\frac{\varepsilon_1}{kT}\right), \qquad (2.10)$$

where ε_1 is the difference in zero-point energy for the reactant and the activated complex, i.e. the activation energy for the process.

By a similar argument, the rate of first-order desorption via an activated complex is given by

$$\frac{dN_g}{dt} = \kappa \frac{kT}{h} \frac{f^*}{f_a} N_a \exp\left(-\frac{\varepsilon_2}{kT}\right), \qquad (2.11)$$

where N_a and f_a refer to the adsorbed species, and ε_2 is the activation energy for the desorption of a single molecule, referred to as the zero-point energy of the adsorbed species.

We may now convert this formalism of the Eyring theory of activated desorption into thermodynamic terms by using that $K^*_{(\text{eq})} \equiv \exp\left(-\Delta G^*/RT\right)$

where $\Delta G^* \equiv \Delta H^* - T\Delta S^*$, where ΔH^* and ΔS^* are respectively the activation enthalpy and entropy for the formation of the activated complex from the reactants. Therefore, for n-th order desorption, with

$$K^*_{(eq)} = N^* N_s^{n-1} / N_a^n , \tag{2.12}$$

this produces a general equation for the desorption rate within the Eyring framework:

$$\frac{dN_g}{dt} = \frac{\kappa}{N_s^{n-1}} \frac{kT}{h} \exp\left(\frac{\Delta S^*}{R}\right) \exp\left(-\frac{\Delta H^*}{RT}\right) N_a^n . \tag{2.13}$$

Since N_s ~ 10^{15} cm^{-2} for most adsorbents, the preexponential factor for desorption may be calculated. Assuming no activation entropy and $\kappa \sim 1$, the preexponential factor $\nu_0^{(n)}$ is

$$\nu_0^{(n)} = kT / hN_s^{(n-1)} . \tag{2.14}$$

Thus, for first order desorption, the preexponential factor is about

$$10^{12.3} \le \nu_0^{(1)} \le 10^{12.8} \quad \mathrm{s}^{-1} \quad (T = 100-300\mathrm{K}). \tag{2.15}$$

When the activated complex is given to two degrees of translational freedom and freely rotated, the term $\exp(\Delta S^*/R)$ will cause a factor of ~10^5 increase for the H_2O molecule in the preexponential factor at 100-300 K, if we assume immobile adsorbate.

2.1.2 Transient surface diffusion

Surface diffusions of adsorbate are generally classified into three different categories. On the one hand it is the stochastic thermal mobility of adsorbed particles, namely Brownian motion. In the absence of external forces it is a stochastic process, reflecting the ceaseless energy fluctuations of a system in thermal equilibrium. When the particles are adsorbed on a homogenous surface and do not interact with each other, this leads to simple random walks.[8,12-16] On the other hand, a gradient of density or chemical potential of adsorbates at the surface induces a transport, which can be described by Fick's law. With increasing time, the resulting surface diffusion will lead to a smearing out of an initial concentration profile.[8,12-16] A further case of surface diffusion is related to the adsorption dynamics and the corresponding dissipation of the adsorption energy. This possible lateral motion of molecules in the process of thermalization is called *transient diffusion*, since it is terminated upon equilibration. The adsorption dynamics and the shape of the potential energy surface experienced by the adsorbate need to be considered in order to understand this phenomenon.[16]

In this thesis, the focus is on the transient diffusion of water molecules. Figure 2.10 shows a schematic view of an adsorbate-substrate interaction potential as a function of along and parallel to the surface. During this non-activated adsorption process, the activation energy for desorption (E_d) becomes identical to the adsorption energy (E_{ad}). As an adsorbate impinges to the surface, it feels a adsorption potential perpendicular to the surface (red curve) and a corrugation potential along the surface (blue curve). In order to bound in this potential well, the adsorption energy must be dissipated to the heat bath of the substrate and the lateral motion of the adsorbate may be induced prior to the accommodation in the thermodynamic equilibrium state. Such transiently mobile adsorbates are designated as *hot precursors* in order to make a distinction to the precursor states introduced above.

Figures and Table

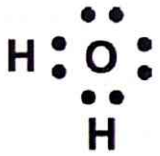

Fig. 2. 1. Lewis structure of water molecule.

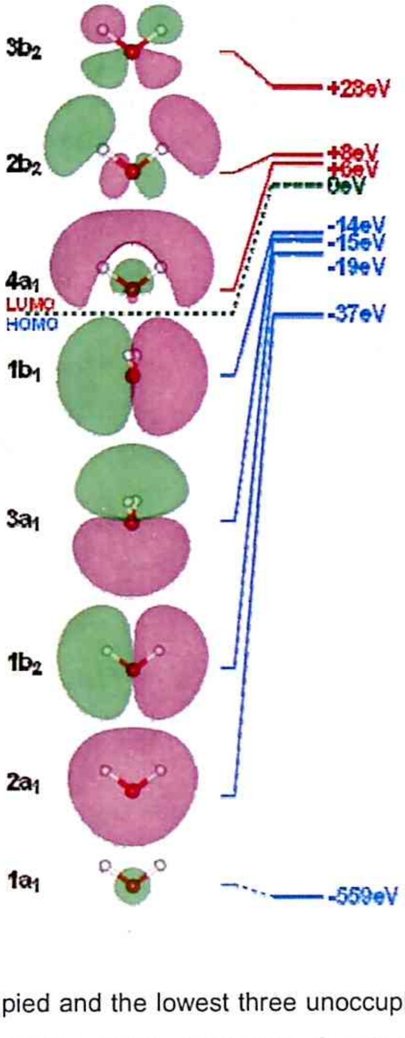

Fig. 2. 2. Calculated five occupied and the lowest three unoccupies MOs of isolated water and their eigenvalues using the Restrictes Hartree-Fock wave function with the 6-31G basis set. [1]

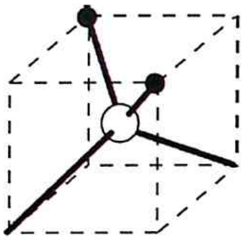

Fig. 2. 3. Schematic representation of the localized MOs of H_2O. The filled circles represent the hydrogen atoms and the open circle represents the oxygen atom.

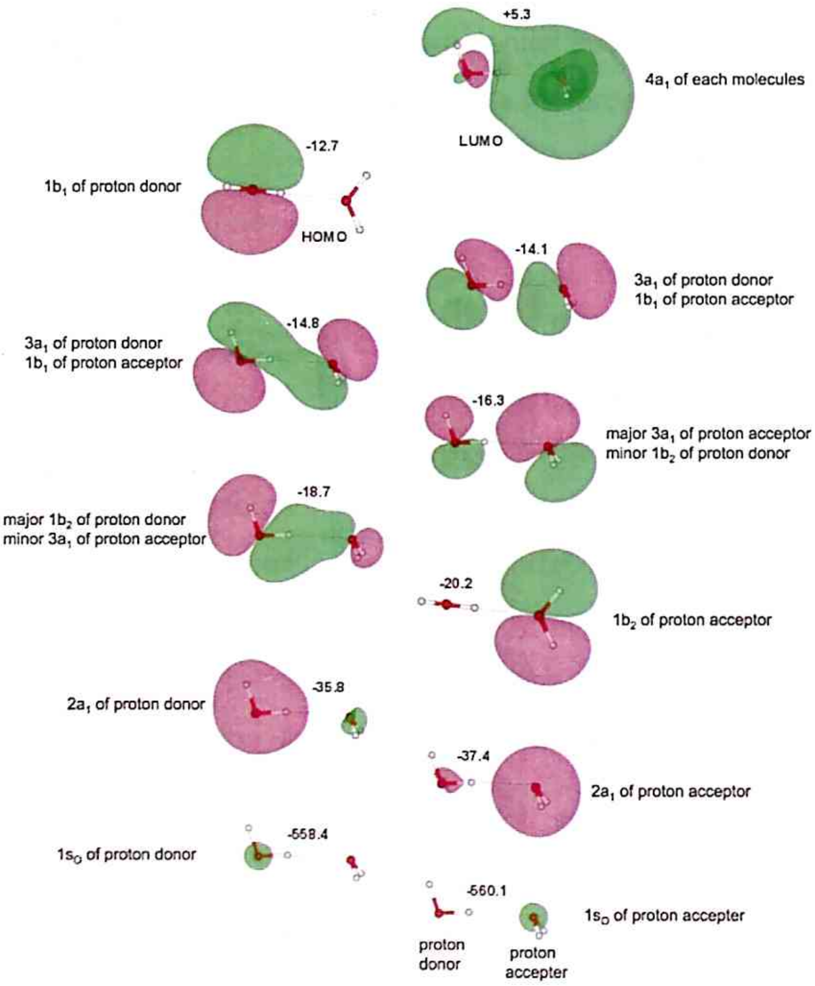

Fig. 2. 4. Calculated MOs of isolated water dimer and their eigenvalues using the Restrictes Hartree-Fock wave function with the 6-31G basis set.[1]

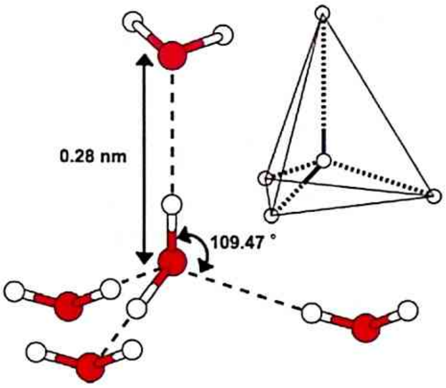

Fig. 2. 5. Arrangement of water molecules in ice. The dashed lines symbolize hydrogen bonds.

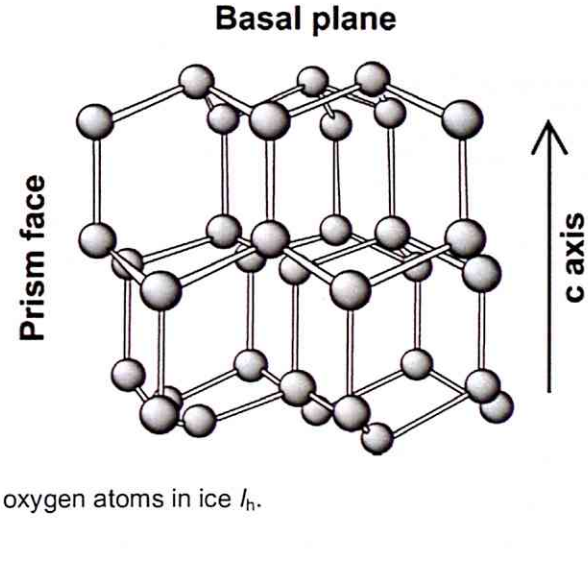

Fig. 2. 6. Positions of oxygen atoms in ice *I*$_h$.

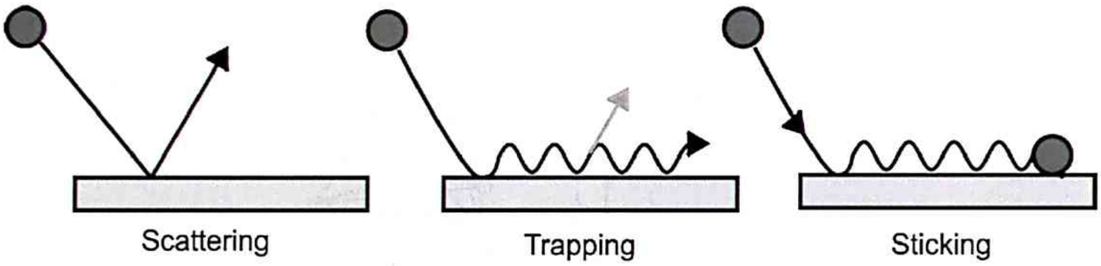

Fig. 2. 7. A schematic of the processes that can occur when a molecule collides with a solid surface.[9]

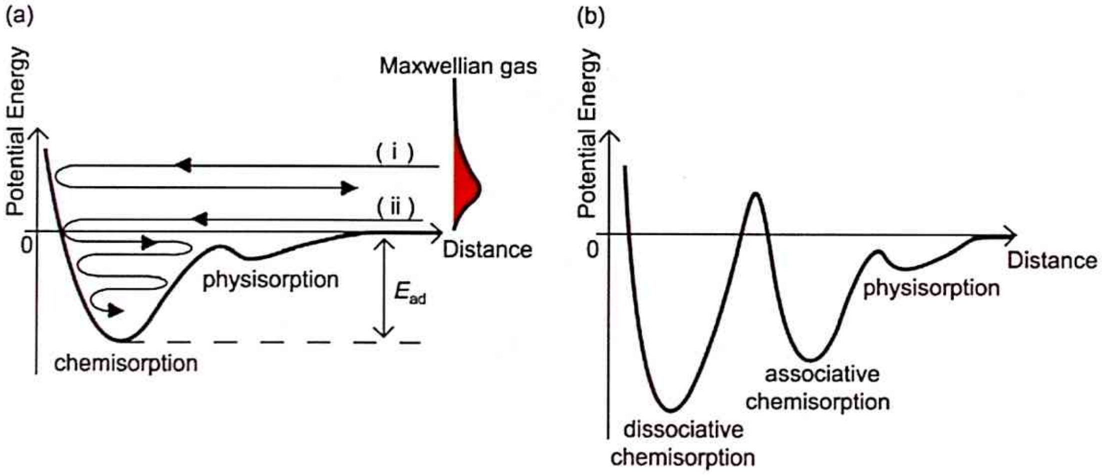

Fig. 2. 8. Schematics of one-dimensional gas-surface interaction potential for chemisorption systems. (a) Non-activated adsorption. (i) and (ii) represent the trajectories of reflected and adsorbed gases, respectively. (b) Activated adsorption.

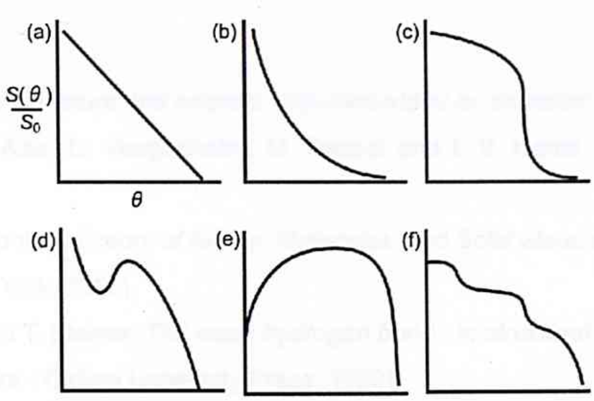

Fig. 2. 9. A general classification of the variation in the sticking probability with coverage.[9]

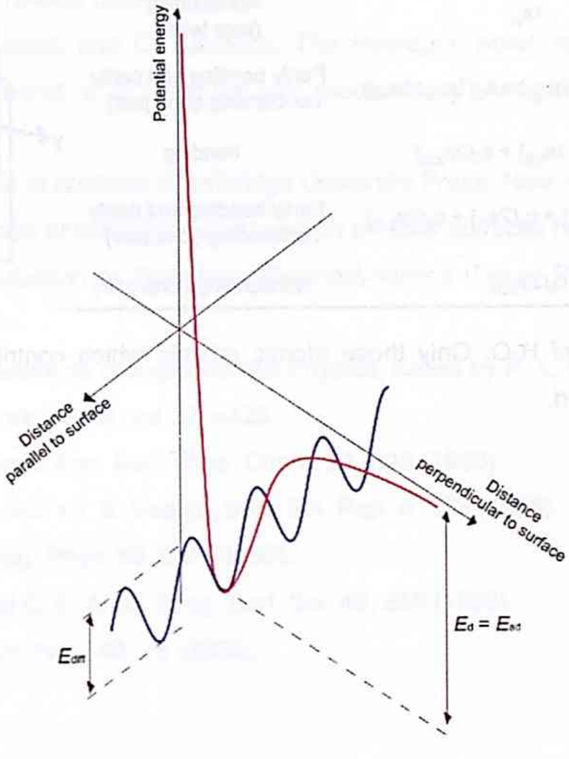

Fig. 2. 10. Schematic view of a adsorbate-surface interaction potential as a function of distance along and parallel to the surface. Red (blue) curve shows a one-dimensional adsorption (diffusion) potential energy surface. The activation energy for surface diffusion is noted as E_{diff}.

MO	Atomic equivalent	Description
$1a_1$	$1s_O$	Nonbonding (core level)
$2a_1$	$c_1(2s_O) + c_2(2p_{z,O}) + c_3(1s_{HA}+1s_{HB})$	Partly bonding and partly nonbonding (lone pair)
$1b_2$	$c_4(1s_{HA}-1s_{HB}) + c_5(2p_{x,O})$	bonding
$3a_1$	$c_6(1s_{HA}+1s_{HB}) + c_7(2s_O) + c_8(2p_{z,O})$	Partly bonding and partly nonbonding (lone pair)
$1b_1$	$c_9(2p_{y,O})$	Nonbonding (lone pair)

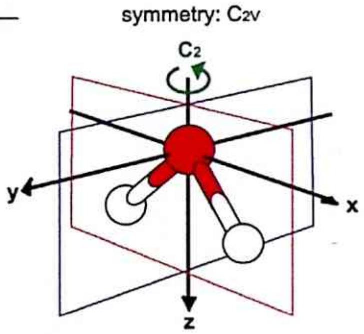

Table 2. 1. LCAOs of H_2O. Only those atomic orbitals which contribute significantrly to the resultant MO are listed.

References

1. M. Chaplin, *Water structure and science*, http://www.lsbu.ac.uk/water/
2. B. Winter, E. F. Aziz, U. Hergenhahn, M. Faubel and I. V. Hertel. J. Chem. Phys. **126**, 124504 (2007).
3. S. F. Boys, in *Quantum Theory of Atoms, Molecules, and Solid State*, edited by P. O. Lowdin, (Academic, New York, 1966).
4. G. R. Desiraju and T. Steiner, *The weak hydrogen bond : in structural chemistry and biology* (Oxford ; New York : Oxford University Press, 1999)
5. D. Eisenberg and W. Kauzmann, *The Structure and Properties of Water* (Oxford University Press, New York, 1969).
6. A. Nilsson, H. Ogasawara, M. Nordlund, M. Nyberg, Ph. Warnet, and L. G. M. Pettersson, J. Chem. Phys. **122**, 154505 (2005).
7. P. Schuster, G. Zundel, and C. Sandorfy, *The Hydrogen bond: recent developments in theory and experiments, v. 2: Structure and spectroscopy* (American Elsevier, New York, 1976)
8. A. Zangwill, *Physics at surfaces* (Cambridge University Press, New York, 1988).
9. R. I. Masel, *Principles of adsorption and reaction on solid surfaces* (Wiley, New York, 1996).
10. T. L. Hill, *An Introduction to Statistical Thermodynamics* (Dover Publications, New York, 1986).
11. J. T. Yates, Jr., in *Methods of Experimental Physics*, edited by R. L. Park and M. G. Lagally, (Academic, New York, 1985), vol.22, p425.
12. G. Ehrlich and K. Stolt, Ann. Rev. Phys. Chem. **31**, 603 (1980).
13. A. G. Naumovents and Yu. S. Vedula, Surf. Sci. Rep. **4**, 365 (1985).
14. R. Gomer, Rep. Prog. Phys. **53**, 917 (1990).
15. E. G. Seebauer and C. E. Allen, Prog. Surf. Sci. **49**, 265 (1995).
16. J. V. Barth, Surf. Sci. Rep. **40**, 75 (2000).

Chapter 3

Experimental

In the present study, IRAS, SPA-LEED, and TPD were used in order to investigate the adsorbed water molecules on the Rh(111) surface. The experimental apparatus, sample preparation, and experimental procedures are described in this chapter.

3.1 The UHV system

A schematic of the UHV chamber used in the present study is shown in Fig. 3.1. The apparatus comprises a cylindrical stainless steel chamber, pumped by a 300 l/s ion pump (IP) (Physical Electronics) which can be isolated by a butterfly valve (VAT), a 345 l/s turbomolecular pump (TMP) (Leybolt), a titanium sublimation pump (TSP) (Physical Electronics), and a non-evaporable getter (NEG) pump (SAES Advanced Technologies). Closing an angle valve (MDC) between the UHV chamber and the TMP brings the vacuum chamber into the closed system, which is evacuated by IP, TSP, and NEG. The sample cooling system is mounted on a rotary stage (θ) (Sinku-Kogaku), which is differentially pumped by an oil diffusion pump (Edwards), and on an XYZ stage (McAllister). The tilt of a sample is also adjustable by the XYZ stage. A Bayard-Alpert gauge (ANELVA) is used to measure the system pressure and a base pressure superior to 1 x 10^{-10} Torr is routinely achieved after baking at 120 °C for about 72 hours. The presented system incorporates a Fourier transform infrared reflection absorption spectrometer (FT-IRAS) (Bruker IFS66v/S), a spot-profile analysis low-energy electron diffraction (SPA-LEED) (Omicron), and a quadrupole mass spectrometer (QMS) (Balzers, QMS200) used for residual gas analysis and temperature programmed desorption (TPD). The chamber is also equipped with an ion gun (Specs, IQE 11) for sample cleaning and a homemade and flood electron gun (Specs, FG 15/40) for electron irradiation. A pulse valve (Parker Hannifin, Series 99) is used for gas dosing into the UHV chamber and directed toward the sample from out-of-plane positions.

3.2 Sample holder

The schematic diagrams and photographs of the sample holder used in this study are shown in Fig. 3.2 and 3.3, respectively. The main body of the sample holder is made of an oxygen free high conductivity (OFHC) copper that is coated with gold to reflect heat radiation and achieve high thermal conductivity.

At the center of the copper (Cu) sample holder, there is a square-shaped window (10 x 10 mm). A sapphire disk (ϕ = 23 mm, thickness t = 1 mm) and a tantalum (Ta) plate (ϕ = 25 mm, t = 0.5 mm), with ϕ 13 and 9 mm holes in the center, and attached on top of the Cu sample holder. The single crystal sample (ϕ = 10 mm) is mounted on the Ta plate by spot welding the sample edge with the Ta plate using a small piece of Ta sheet, while the whole set of the sample, sapphire disk, and Ta plate is rigidly fixed to the Cu sample holder by molybdenum (Mo) screws, washers, and nuts, which provides mechanical.

The sample mounted on the Ta plate is electrically isolated from the grounded Cu sample holder by sapphire disk and ceramic tubes. A Cu wire insulated with a polyimide tube is connected to one of the electrically isolated Mo screws, which allows biasing of the sample at a fixed electric potential. Consequently, the sample current can be measured during electron bombardment, ion sputtering, and electron irradiation. It should be noted that the sample current is measured over the area of the Ta plate ($\phi = 25$ mm) because the whole Ta plate, including the sample crystal, is electrically connected.

Near the rear-side of the sample, a 0.15 mm diameter thoriated tungsten (W) filament is located, which is used to heat the sample radiatively and/or by electron bombardment.

A chromel-alumel (K-type) thermocouple is spot welded to the side of the sample to monitor the sample temperature. Note that a different diameter thermocouple is used (0.05 mm) near the sample to reduce the heat inflow.

There are two silicon diodes (Lake Shore Cryotronics, DT-470-SD-12) measuring the temperatures at the bottom of a cryostat cold head (Si diode A) and at the middle of the Cu sample holder (Si diode B). Note that the temperature of a Si diode must never exceed 156 °C, which is the melting point of the indium solder used for its connection.

All the electrical wires are thermally anchored by being wound around the cryostat rod in order to minimize the heat to the sample from the room temperature feedthroughs. In addition, the entire sample holder is covered with a Cu radiation shield, which suppresses the direct thermal radiation from the room temperature chamber wall.

3.3 Sample preparation

The rhodium (Rh) single crystal (purity 99.99 %, Surface Preparation Laboratory) was cut to within 0.4 ° of the (111) face, and had a diameter of 10 mm and thickness of 2 mm.

The Rh(111) single crystal surface was cleaned by cycles of Ne ion sputtering, flashing and annealing. In each sample cleaning cycle, the sample was sputtered by Ne ions for 30 min in the following conditions: E = 500~800 eV, P_{Ne} = 4~6 x10^{-6} Torr, and the sample current density I= 0.3~0.4 μA/cm^2. After ion sputtering, the sample was flashed to 1300 K several times and subsequently annealed at 1000 K for 5 min. These procedures produced a well ordered surface, which was characterized by sharp and low background (1x1) LEED spots as shown in Fig. 3.4. At the final stage of sample cleaning, the sample was exposed to oxygen at 300 K followed by flashing of the sample to 1300 K, with this oxygen treatment repeated cyclically several times. The cleanness of the Rh(111) surface was checked by the adsorption behavior of water and CO in IRAS,[1,2] and TPD of water.[1] If carbon exists on the surface, adsorbed CO may be observed by the reaction of carbon with post–dosed oxygen in this experiment. After careful cleaning, no such CO species was observed on the Rh(111) "clean" surface by IRAS. Thus, considering the sensitivity of IRAS (typically 1/1000 of CO ML), the coverage of carbon atom impurities was estimated to be less than 0.001 ML on the clean surface and the amount of defects on the Rh(111) surface is estimated to be less than 0.5% (see chapter 5).

All the molecules were introduced onto the sample surface through a pulse gas dosing system. The pulse valve is a solenoid valve, whose opening duration is controllable by the pulse duration of the input TTL signal. The pulse duration ranges from microseconds and milliseconds, although longer periods can be selected. The gaseous molecules were guided from the pulse valve to the vicinity of the sample surface via a stainless steel tube with an internal diameter of 1/8 inch. This pulse gas dosing system exhibits the following advantages in comparison to the usual procedure of backfilling the UHV chamber using a variable leak valve. Firstly, the pulse duration, the number of shots, and the gas line pressure can precisely control the exposure. The usage of a variable leak valve is associated with relatively large error because of its manual operation. Secondly, using a guide tube it is possible to deliver the molecules locally onto the sample surface, and thus minimize the deterioration in the vacuum pressure. This advantage is especially important in water experiments because it takes considerable time to pump out water molecules after exposure.

All the isotopic waters, $H_2{}^{16}O$ (Milli-Q), $D_2{}^{16}O$ (Aldrich, isotopic purity 99.96 %) and $H_2{}^{18}O$ (Isotec, isotopic purity 95.5 %), were degassed through several freeze-pump-thaw cycles prior to exposure and the purity was also checked using the IRAS and QMS.

3.4 Sample cooling system

The sample was cooled by a continuous flow liquid He cryostat (Advanced Research Systems, Helitran LT-3B). Liquid He was supplied by a flexible transfer line connected to a He Dewar but liquid N_2 may also be used.

The unique designs of Helitran make it possible to perform experiments with no vibrations induced by cavitation, which results from a boiling of the liquid in the transfer line as well as the cryostat, and which is so common in standard helium transfer systems. No vibration at the sample is especially important in IRAS because any deviation in the sample position significantly affects the intensity of a reflected IR beam at the detector.

30 minutes will be required from the beginning to cool after the liquid He starts to flow. Once the cooling starts, the sample temperature dropped from room temperature to the minimum temperature (20 K) in 15 min.

The minimum temperatures at the bottom of a cryostat cold tip (measured by a Si diode A) and at the middle of the Cu sample holder (Si diode B) were 6.1 K and 8.3 K, respectively, while the lowest temperature of the sample was 20 K (measured by a K-type thermocouple).

The temperature was regulated by adjusting the cryogen flow rate with a needle valve and by a heater wrapped around the cold tip (see Fig. 3.2). The heater is controlled with a temperature controller (Lakeshore, Model 331). The low heat loss rate of the transfer line permits sample temperature stability of ±0.01 K and the small usage of the cryogen (1-2 liter per hour) at the minimum temperature.

3.5 Temperature calibration

The temperature calibration for a K-type thermocouple is required at a low temperature, which is because the thermocouple voltage and electromotive force (EMF) of a K-type thermocouple exhibits a small temperature response at low temperature as compared at room temperature: 2 μV/K at 10 K and 40 μV/K at 300 K. Thus, a substantial error in the temperature measurement would be caused by the deviation of EMF resulting from the following factors:

- The temperature fluctuation in a reference point of the thermocouple.
- The exact composition of the thermocouple at the junction to the sample. The composition at the joint point to the sample may be altered by spot welding and/or high-temperature treatment in the sample cleaning

procedures. In addition, the composition of a thermocouple alloy varies depending on the manufacturers involved.

Furthermore, if the actual junction of the thermocouple is not on the sample, the observed temperature may differ from the true sample temperature.

Therefore, an *in situ* temperature calibration is required to create an EMF-temperature curve specific to each experimental setup. The temperature calibration was performed using the common leading edges of the multilayer desorptions of O_2, Kr, Xe and CO_2. The temperatures of the common leading edges are 26 (O_2), 32 (Kr), 46 (Xe), and 80 (CO_2) K.[3,4]

Figure 3.5 shows the standard EMF-temperature curve for a K-type thermocouple (JIS C 1602). In this figure, the observed values of the thermocouple voltages at the common leading edges of O_2, Kr, Xe and CO_2 multilayers are plotted against the reported temperatures.[3,4] Above 80 K, the standard EMF-temperature gives correct temperature. Below 80 K, calibration data points were fitted using 6th order polynomial equation which is shown as dashed line in the figure. By extrapolating the thermocouple voltage of this sample, the minimum temperature was estimated to be 20 K.

3.6 IRAS

A top view of the IRAS system is shown in Fig. 3.6. The IRAS system consists of an FTIR spectrometer, optics, a UHV chamber, and IR detectors.

A Bruker IFS66v/S FTIR spectrometer, used in this study, contains an IR source (a Globar lamp) and a 45° Michelson interferometer. The IR radiation emitted from the Globar lamp goes through an aperture; the effective size of the IR source is determined by the aperture size. The IR beam is collimated by the mirror M2 before entering the interferometer. In the interferometer, Germanium-coated KBr wafers are used as a beam splitter and a moving mirror (M4) in the interferometer is operated by an air bearing, which ensures stable mirror travel throughout each scan. The IR beam is reflected by the planar mirrors (M5 and M6) and focused onto the sample in a UHV chamber, such that the incident/reflected angle is 84° with respect to the surface normal. The focusing mirror (M7) is a 90° off-axis parabolic mirror with a focal length of 300 mm (f = 300).

The reflected IR beam is collected and refocused onto the IR detectors. There are two different IR detectors: a mercury-cadmium-telluride (MCT; HgCdTe) detector and a B-doped silicon (Si:B) detector. The MCT detector is an intrinsic photoconductive detector operating at liquid N_2 temperature and with a measurable wavenumber region of 7500-700 cm^{-1}. The detector window is ZnSe. On the contrary, the Si:B detector is an extrinsic photoconductive detector operating at liquid He temperature. The measurable wavenumber region is 4000-370 cm^{-1}. The detector window is KRS-5 and switching between MCT and Si:B detectors is enabled by moving the mirror M10. The output signal from the detector is amplified and transferred to a data acquisition board on the PC via the Bruker FTIR spectrometer.

The entire IR optics is evacuated down to 1 mbar by an oil-free scroll pump (ANEST IWATA, ISP-250B). This evacuated optics enables the removal of atmospheric absorptions, such as a gaseous water (H_2O) and carbon dioxide (CO_2), from the IRAS spectra. The UHV chamber and evacuated IR optics are separated from each other by KBr windows through which the incident/reflected IR beams pass.

Using this IRAS system, one can obtain IRAS spectra with low noise levels and without any influences of atmospheric gases remaining in the IR optics. Figure 3.7 shows the IRAS spectra with 4 cm^{-1} resolution and 500 scans using (a) MCT and (b) Si:B detectors. The rms (root mean square) noise levels in the spectral region of 2000-2200 cm^{-1} are 7.2 x 10^{-6}, 6.0 x 10^{-6} Absorbance for MCT and Si:B detectors, respectively. Note that these IRAS spectra do not exhibit any absorptions of atmospheric gases such as H_2O and CO_2. The water vapor has rotation-vibration bands centered near 3750 and 1650 cm^{-1}, and the bands of CO_2 vapor are located near 2350 and 668 cm^{-1}.[5]

The Si:B detector can detect lower frequency vibrations than the MCT detector. The detection of low frequency vibrations is made possible, not only by the Si:B detector itself but also by optical devices, including a KBr beamsplitter, KBr windows, and a KRS-5 detector window. A KBr has a high transmissivity of ~90 % over the spectral range from 0.23 to 25 μm (from 43500 to 400 cm^{-1}).[6] In addition, a KRS-5 has transmissivity of ~70 % over the spectral range from 0.6 to 40 μm (from 16500 to 250 cm^{-1}).[6]

3.7 SPA-LEED

SPA-LEED was developed by M. Henzler and his group at the University of Hannover.[7] Besides the optics in the conventional LEED, a CEM detector (channel electron multiplier), deflection plates, and an entrance lens are equipped as shown in Fig. 3.8. The diffraction pattern is scanned over the channeltron aperture by applying voltages to the octapole deflection plates. No mechanical movements of the sample and the detector are required during scanning. The intensity at a given position of the pattern is detected by the channeltron. SPA-LEED can be used as a conventional LEED with its phosphor screen.

The experimentally measured intensity function will always be broadened by the instrumental response function. The instrumental response width of a LEED system consists of four major contributions: the energy spread of the incident electron beam, the aperture width of the detector, the source extension, and the electron beam diameter.[8] The response width may be regarded as the uncertainty associated with the measurement of position in a reciprocal space, each of which contributes individually to the overall uncertainty. The SPA-LEED system suppresses these contributions using a lanthanum-hexaboride (LaB_6) filament as a cathode, the entrance lens for additional focusing of the primary and diffracted beams, and the entrance aperture of the detector. Consequently, the SPA-LEED system shows a transfer width, which is the maximum distance of surface atoms for a coherent diffraction, of about 1000 Å, compared to a transfer width of a conventional LEED system of about 100 Å.[8]

3.8 TPD

In TPD measurements, the sample temperature is ramped and the rate of desorption is measured by monitoring the partial pressure of adsorbates desorbed into the gas phase as a function of temperature. The desorbing molecules are detected by a QMS (Balzers QMS 200) with a Faraday cup or a secondary electron multiplier (SEM) detector, while the ionization volume of the detector is enclosed in a home-built small glass envelope ("Feulner cup").[9]

When the TPD spectra are measured, the single crystal surface is placed in front of a compact (3.4 mm diameter) opening of a glass cup at a distance of 2 mm. The advantage of this setup is the excellent signal-to-background ratio since the QMS ionization source selectively detects the desorbing molecules from the sample surface.

The temperature control of the sample is performed with a home-built temperature controller and the proportional feedback temperature controller applies power to a tungsten filament in proportion to the difference between the measured and programmed temperatures. The sample can be heated not only by thermal radiation from the rear-located tungsten filament (with the grounded sample) but also electron bombardment from the filament (with the biased sample).

Figures

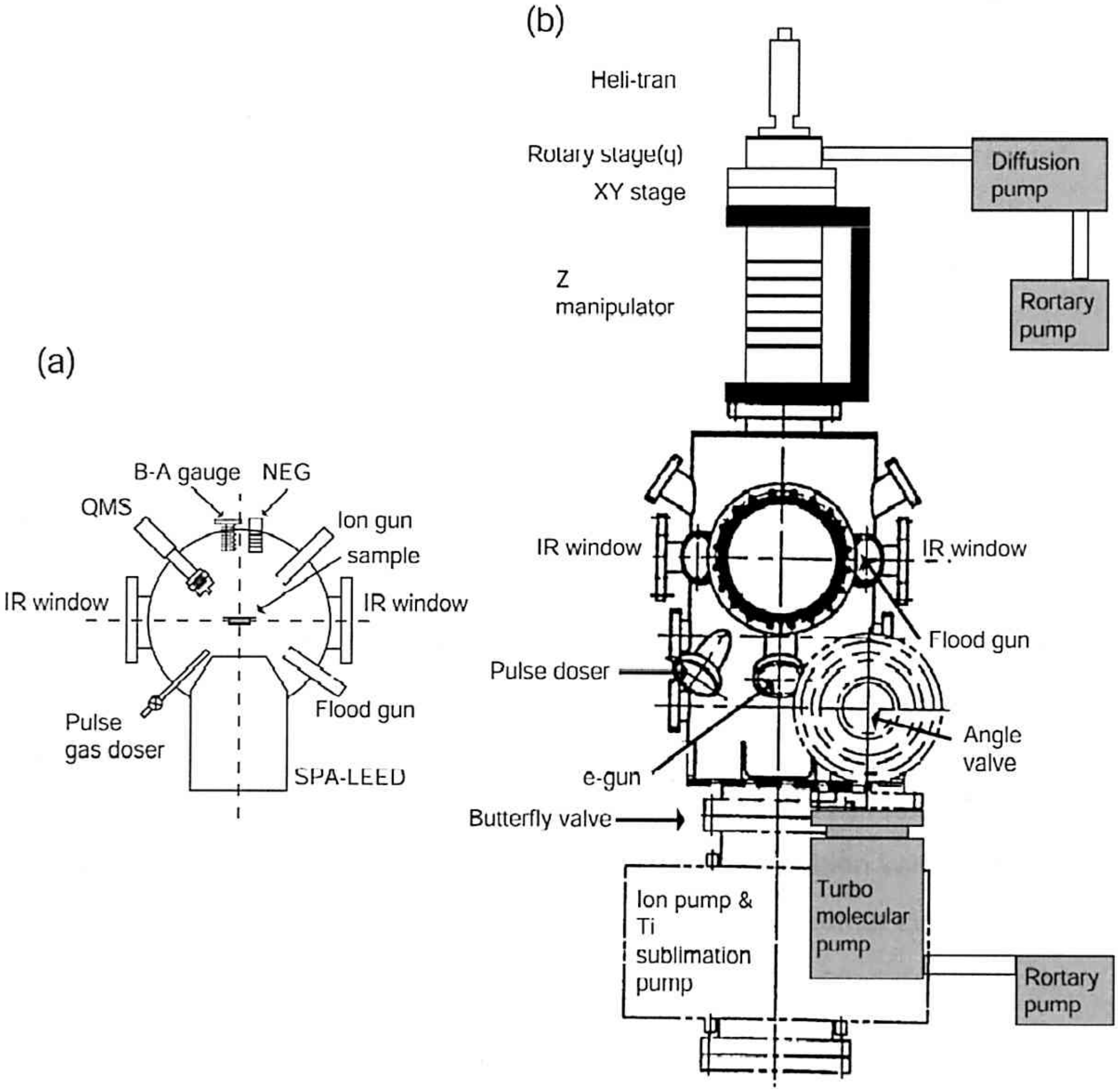

Fig. 3. 1. Schematic diagram of the IRAS/SPA-LEED chamber. (a) top view, and (b) side view.

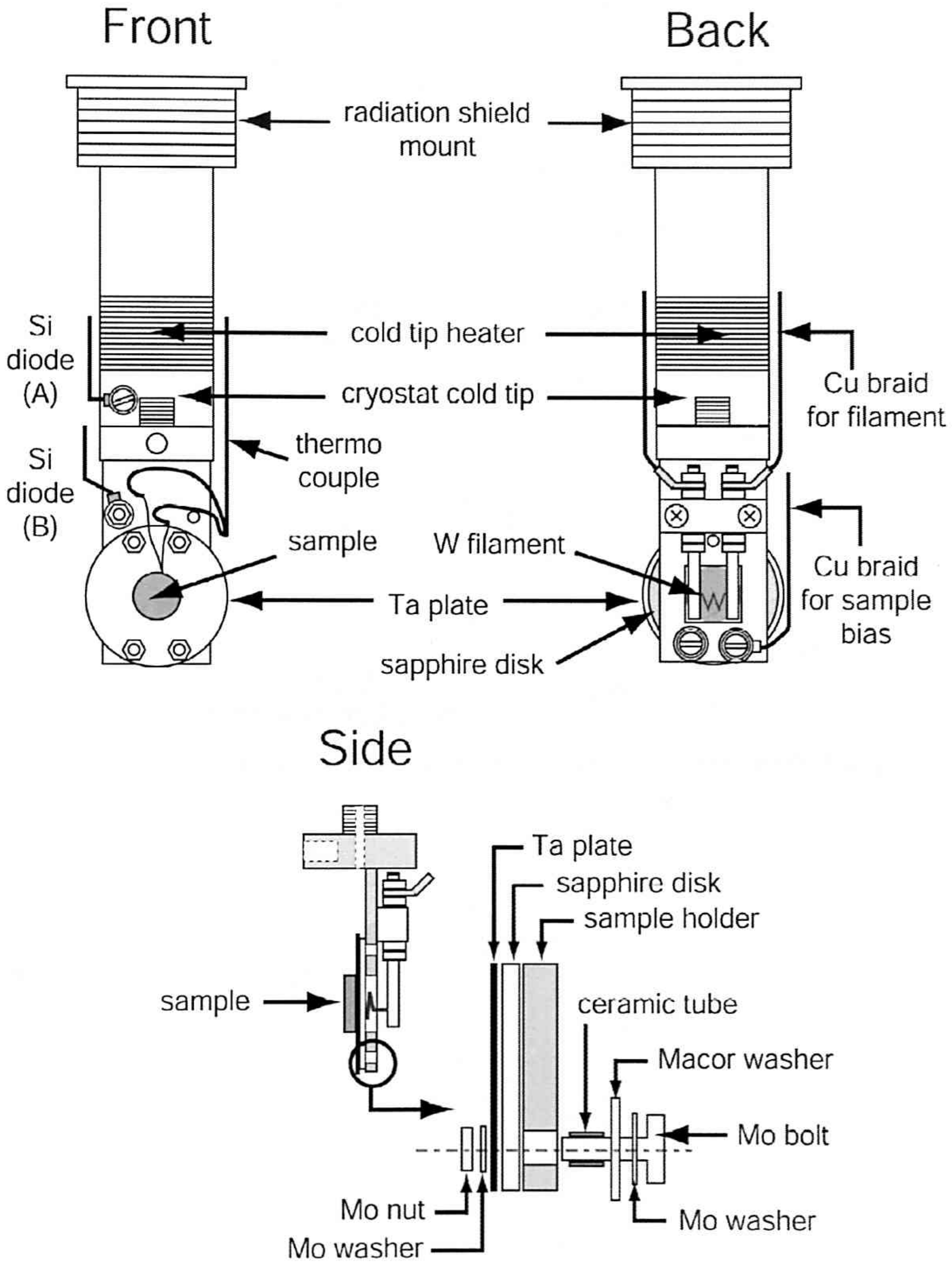

Fig. 3. 2. Schematic diagram of the sample holder for the IRAS/SPA-LEED system.

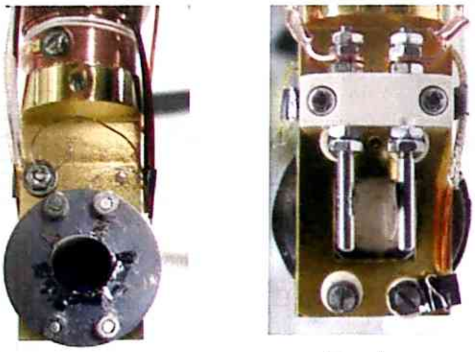

Front

Back

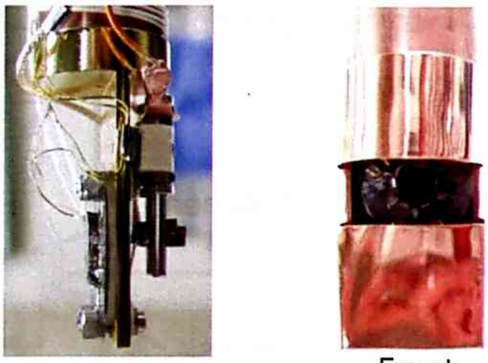

Side

Front
(with radiation shield)

Fig. 3. 3. Photographs of the sample holder for the IRAS/SPA-LEED system.

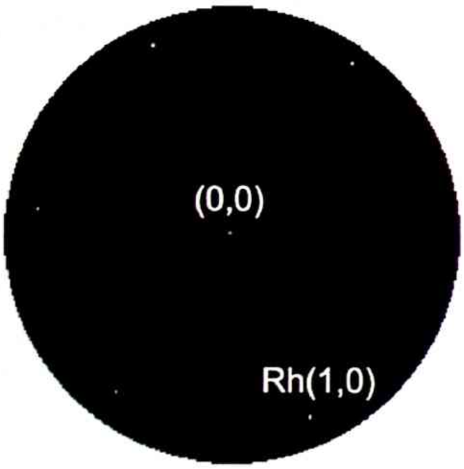

Fig. 3. 4. LEED pattern of the Rh(111) surface observed at 20 K (E_p = 120 eV).

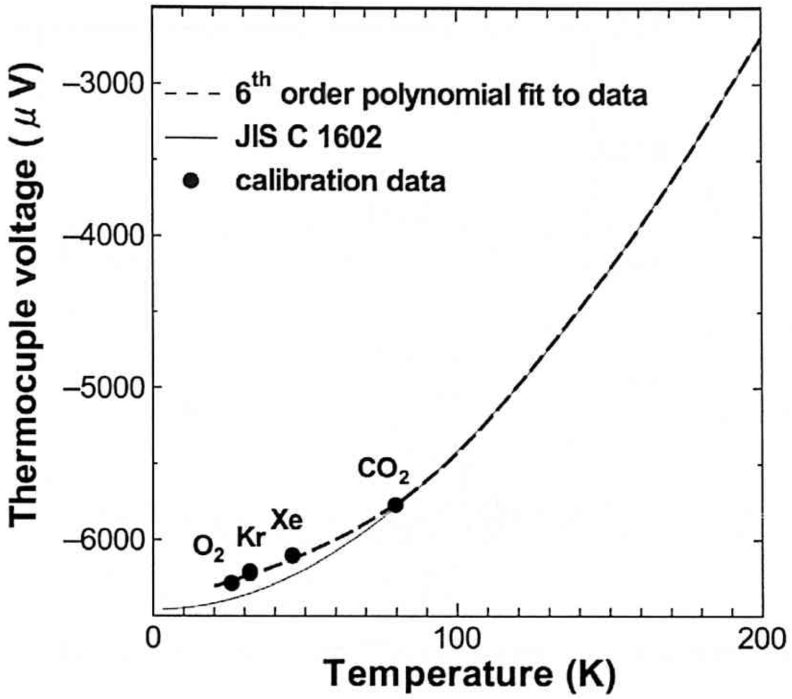

Fig. 3. 5. The standard thermocouple voltage-temperature curve (JIS C 1602) for a K-type thermocouple (solid line) and the temperature calibration data (closed circle). The dashed line is fitted by 6th order polynomial equation for data points (<80 K).

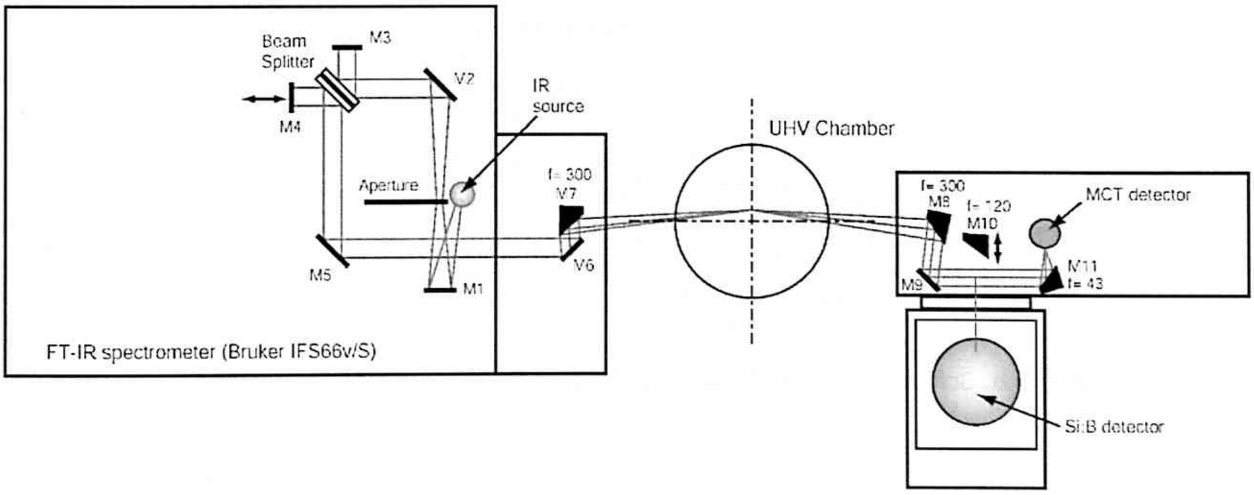

Fig. 3. 6. Optical configuration of the IRAS system.

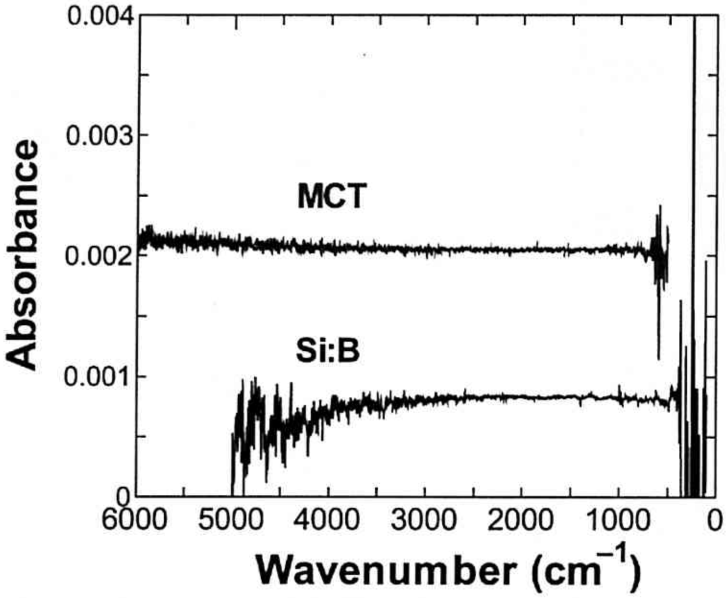

Fig. 3. 7. FT-IRAS spectra measured by (a) MCT and (b) Si:B detectors (Resolution 4 cm^{-1} and 500 scans).

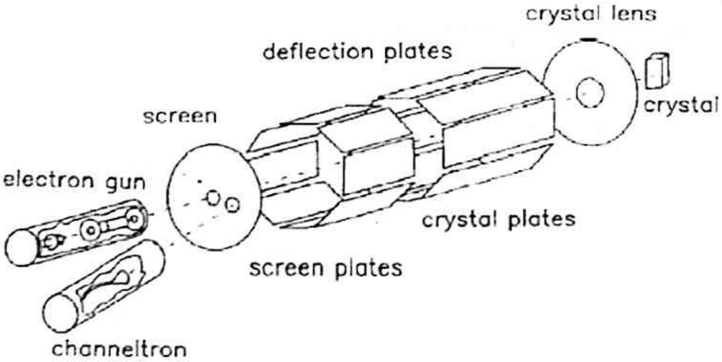

Fig. 3. 8. Schematic set up of the SPA-LEED system.

References

1. F. T. Wagner and T. E. Moylan, Surf. Sci. **191**, 121 (1987).
2. R. Linke, D. Curulla, M. J. P. Hopstaken, and J. W. Niemantsverdriet, J. Chem. Phys. **115**, 8209 (2001).
3. H. Schlichting and D. Menzel, Rev. Sci. Instrum. **64**, 2013 (1993).
4. M. J. Weida, J. M. Sperhac, and D. J. Nesbitt, J. Chem. Phys. **105**, 749 (1996).
5. P. R. Griffiths and J. A. de Haseth, *Fourier transform infrared spectroscopy* (Willey, New York, 1986).
6. Janos Technology, web: http://www.janostech.com/
7. U. Scheithauer, G. Mayer, and M. Henzler, Surf. Sci. **178**, 441 (1986).
8. M. A. Van Hove, W. H. Weinberg, and C-. M. Chan, *Low-Energy Electron Diffraction* (Springer, Berlin, Heidelberg 1986).
9. P. Feulner and D. Menzel, J. Vac. Sci. Technol. **17**, 662 (1980).

Chapter 4

Basic principles

In the present study, IRAS, SPA-LEED, and TPD were used in order to investigate the adsorbed water molecules on the Rh(111) surface. IRAS is used to probe the vibrational properties of adsorbed molecules, while SPA-LEED measurements provide quantitative spots analysis and high-resolution diffraction patterns. Using TPD, the desorption kinetics and relative coverage of adsorbate are addressed.

4.1 Infrared reflection adsorption spectroscopy[1-5]

IRAS is a very useful technique to study vibrational excitations of the atoms and molecules adsorbed on metal surfaces. In IRAS a beam of infrared photons is incident on a surface covered by molecules. Some of the photons are absorbed in the adsorbed layers while those remaining are either reflected or absorbed by the underlying substrate. A characteristic "dip" will be observed at those energies of the incident photons, which corresponds to the vibrational excitation energies of the adsorbates.

Consider the reflection of infrared radiation from a clean and highly reflecting metal surface. The incident beam impinges at an angle ϕ relative to the surface normal: the incident and reflected beam and the surface normal lie in the incident plane (Fig. 4.1). The interaction of the light with the surface is described by the Fresnel equations, which incorporate the appropriate boundary conditions in the electromagnetic wave equations of the incident, reflected, and the refracted wave fronts, providing the amplitude r and phase δ of the reflected wave with respect to the incident in terms of the complex index of refraction $\tilde{n} = n + ik$ of the phases making up the interface. The amplitude and phase changes experienced on reflection depend upon the direction of the electric field vector of the wave fronts, and it is convenient to resolve the electric field vector into components in the incident plane (P polarized) and normal to the incident plane (S polarized) (Fig. 4.1), likewise resolving the reflection coefficients (r_s and r_p) and phase changes (δ_s and δ_p) yielded in the Fresnel's equations. If $n^2 + k^2 >> 1$, which is true for metals in the infrared wavelength region, the following formulas can be derived:

$$R_p = r_p^2 = \frac{(n - \sec\phi)^2 + k^2}{(n + \sec\phi)^2 + k^2} \tag{4.1}$$

$$R_s = r_s^2 = \frac{(n - \cos\phi)^2 + k^2}{(n + \cos\phi)^2 + k^2} \tag{4.2}$$

$$\Delta = \delta_p - \delta_s = \arctan\left(\frac{2k\tan\phi\sin\phi}{\tan^2\phi - (n^2 + k^2)}\right) \tag{4.3}$$

where R_p and R_s are the intensity coefficients, δ_s and δ_p the phase shifts on reflection, and ϕ is the angle of incidence (Fig. 4.1).

Figure 4.2 shows a plot of R_p and R_s, δ_s and δ_p as a function of ϕ under the appropriate conditions of a highly reflecting metal in the infrared (n = 3, k = 30). The electric field at the surface is the vector sum of the electric field components due to the incident, reflected, and refracted waves. The optical properties of the metal ($n^2 + k^2 >> 1$) lead to the majority of the incident intensity being reflected, and a negligible contribution of the refracted waves to the surface electric. If the amplitude of the incident electric field is $E^i \sin\theta$ (where θ is an arbitrary phase), the field due to the reflected wave is $E^i r \sin(\theta + \delta)$. The resulting field at the surface is therefore given by

$$E = E^i [\sin\theta + r\sin(\theta + \delta)] \tag{4.4}$$

The *P* and *S* polarized electric field components can be considered separately as before, and we are interested in the direction of the resulting surface electric field E_p or E_s with respect to the metal surface. Note that for all incident angles ϕ, E_s^i and E_s^r remain parallel to the surface (Fig. 4.1), i.e. the resulting electric fields, which are parallel to the metal surface, are given by $E_s = E_s^i + E_s^r$, and from equation (4.4) we have

$$E_s = E_s^i [\sin\theta + r\sin(\theta + \delta_s)] \tag{4.5}$$

Since δ_s is close to 180° and $r_s \approx 1$ for all ϕ (Fig. 4.2) it can be seen from equation (4.5) that the 180° phase change leads to destructive interference and a vanishingly small electric field at the surface. No interaction of the surface electric field due to E_s with surface dipoles is possible. P polarized radiation, however, behaves quite differently since the incident and reflected electric wave fields have components both parallel and normal to the surface (inset in Fig. 4.3) and sum to yield parallel $E_p^{//}$ and normal $E_p^{\perp}$ components of the surface electric field given by

$$E_p^{//} = E_p^i \cos\phi [\sin\phi - r_p \sin(\theta + \delta_p)] \tag{4.6}$$

$$E_p^{\perp} = E_p^i \sin\phi [\sin\phi + r_p \sin(\theta + \delta_p)] \tag{4.7}$$

Note that for a wide range of angles ϕ, δ_p remains small (Fig. 4.2) and only increases to -180° near grazing incidence. The parallel components of E_p^i and

E_p^r combine to give a very small resultant field $E_p^{//}$ at low angles, even though they are in phase, similar in magnitude (r_p ~ 1), and their contribution to E_p is largest [cosϕ term in equation (4.6)] simply because they are in the opposite direction. The normal components combine constructively [equation (4.7)] but at low angles $E_p^{\perp}$ remains small because only a small proportion is resolved in the surface normal direction [sinϕ term in equation (4.7)]. As ϕ increases, so do these normal components, with a concomitant decrease in the parallel component. Constructive interference yields a normal component of $\sim 2E_p^i$ before the sharp change in phase towards -180° (Fig. 4.2) causes mutual cancellation [equation (4.7)]. The effect of ϕ on the component $E_p^{\perp}$ is shown in Fig. 4.3 again for reflection from a metal with $n = 3$, $k = 30$. One must conclude, therefore, that incident P polarized radiation can give rise to significant electric fields at the metal surface, but only in a direction normal to the surface, and only at grazing angles of incidence (high ϕ).

Once the enhanced electric field $E_p^{\perp}/E_p^i$ is calculated, one notes that the number of molecules with which the incoming incident ray can interact is proportional to secϕ, and the absorption intensity is proportional to $\left(E_p^{\perp}/E_p^i\right)^2$. Therefore the total absorption intensity in the IRAS experiment is given by $\Delta R = \left(E_p^{\perp}/E_p^i\right)^2 \sec\phi$, the function plotted in Fig. 4.3. This function has the same shape for all metals reflecting in the infrared, but ΔR is largest for highly reflecting metals, which explains why IRAS experiments are carried out at grazing incidence.

Consider a metal surface on which molecules are adsorbed. Assume initially that the molecules do not interact with each other. The interaction energy between one of the molecules and the electric field can be written

$$H' = -\mu \cdot \boldsymbol{E} \tag{4.8}$$

where μ is the dipole moment operator of the molecule. This interaction Hamiltonian is a good approximation since the wavelength of the incident electromagnetic wave is much larger than the size of a molecule. The probability per unit time, w, for the molecule to get excited from its ground state $|i\rangle$ to an excited state $|f\rangle$ with energy $\hbar\Omega$ is given by the Golden rule

$$w = \frac{2\pi}{\hbar^2}\left|\langle f|H'|i\rangle\right|^2 \delta(\Omega - \omega) \tag{4.9}$$

The matrix element $\langle f|H'|i\rangle$ must be totally symmetric with respect to all symmetry operations of a surface point group to have a non zero value of w. This is satisfied if the product $\langle f|i\rangle$ transforms as H'. H' has a component which transforms as z, where the z-axis is normal to the surface. In all two dimensional surface point groups, z transforms as totally symmetric, thus the product $\langle f|i\rangle$ must have a totally symmetric component. The vibrational ground state wave function transforms as the totally symmetric irreducible representation, meaning the excited state must be totally symmetric. This is the surface selection rule for IRAS.

The surface selection rule is entirely equivalent to the result obtained using image dipole theory. The image dipole theory of the surface selection rule is expounded in Fig. 4.4. The long-range electromagnetic field of the infrared radiation cannot distinguish the dipole and its image, and interacts with the sum of their dipole fields. In the case of a perpendicular dipole [Fig. 4.4 (a)] this leads to an increased response (and hence absorption). In the case of a dipole parallel to the surface, the net summation yields only a quadrupole component, and no dipolar field remains for interaction [Fig. 4.4 (a)].

4.2 Spot-profile-analysis low energy electron diffraction[6-11]

Electrons with energies between about 10 and 1000 eV are ideally suited to investigate the topmost layers of solids, because their mean free path in solids is of the order of only a few atomic layers. The characteristic dependence of this property on the electron energy can be seen in Fig. 4.5. The general features of this curve are quite universal for a large number of different materials. A minimum in the free path of only a few hundred pm occurs at energies between 40 and 120 eV. The mean free path increases steeply at energies below 20 eV, but only slowly towards higher energies, and remains <2000 pm at 1000 eV. This behavior forms the basis of the surface sensitivity of LEED, which is the most common technique used in studies of single crystal surfaces. It probes the long-range order of periodic surface structures and also yields valuable information on partially disordered systems, as well as in many cases where a complete structural analysis is not performed.

The interference of slow electrons elastically scattered from a single crystal surface causes their intensity to depend on the direction and electron energy. Analysis is usually performed along the following lines:

(a) Determination of the directions of the interference maxima is possible by inspection of the LEED pattern. Application of the single geometric theory of diffraction then provides the unit cells of the periodic structure elements on the surface.

(b) Only a perfect instrument and an ideally periodic surface will yield diffracted intensity exactly in well-defined orientations. In all other cases the intensity will vary more or less smoothly with angle near these preferred directions. Such “beam profiles” can be analyzed to an effective approximation by applying kinematic theory, which yields information on partial disorder on the surface.

(c) Variation of the primary electron energy yields intensity/voltage (I/V)-spectra for each of the diffracted beams, which forms the basis of a complete structural analysis, i.e. the determination of atomic positions within the unit cell of a periodic surface structure. This requires the elaborated application of dynamical theory.

The kinematic theory of scattered intensities is based on the assumption that the incident radiation interacts with matter only very weakly, so that only the single scattering processes need be considered to give a good approximation. The incident beam of electrons is represented by a plane wave with an initial wave vector $\boldsymbol{k}_i$. After scattering at the surface, the reflected beam of electrons is represented by a final wave vector $\boldsymbol{k}_f$ and the amplitude of a scattered wave is described by the summation of all waves coming from the crystal atoms.

$$\varphi(\boldsymbol{r}) = \left[\sum_j f_j(\boldsymbol{k})\exp(i\boldsymbol{k}\cdot\boldsymbol{r}_j)\right]\exp(i\boldsymbol{k}\cdot\boldsymbol{r}) \qquad (4.10)$$

where $\boldsymbol{r}_j$ is the position of atoms, $\boldsymbol{k} = \boldsymbol{k}_i - \boldsymbol{k}_f$ is the scattering vector, and $f_j(\boldsymbol{k})$ is the atomic scattering factor. If the sample is described by the repetition of identical units,

$$\boldsymbol{r}_j = \boldsymbol{t}_n + m_1\boldsymbol{a}_1 + m_2\boldsymbol{a}_2 \qquad (4.11)$$

where $\boldsymbol{a}_1$ and $\boldsymbol{a}_2$ are the unit vectors of the two dimensional lattice and $\boldsymbol{t}_n$ is the position of the atom in the unit cell. The absolute square of the amplitude, I, is given by

$$I = FG \qquad (4.12)$$

$$F = \left|\sum_n f_n(\boldsymbol{k})\exp(i\boldsymbol{k}\cdot\boldsymbol{t}_n)\right|^2 \qquad (4.13)$$

$$G = \left| \sum_{m_1, m_2} \exp\left[i\boldsymbol{k}_{//} \cdot (m_1\boldsymbol{a}_1 + m_2\boldsymbol{a}_2)\right] \right|^2 \tag{4.14}$$

where F is called the atom factor (for single atoms) or the structure factor or brick factor (for groups of atoms). The factor F contains all information on the scattering properties of a single atom. Since it describes the outgoing wave, it also includes multiple scattering. The second factor G is called the interference factor or lattice factor and is simply due to the repetition of identical units. It does not contain any information about the scattering properties of the atoms or group of atoms and reproduces only the arrangement of identical scatters. Therefore this factor is safely calculated within the kinematical model. For periodic or near periodic lattices the lattice factor has appreciable values only for the definite angles and their immediate neighborhood (spot pattern). The F factor varies slowly with angle compared to G, thus the existence and shape of a spot are completely explained by G. This means the unit mesh in size and orientation is derived from the existence of diffraction spots completely within kinematic approximation. Additionally the spot shape, such as splitting or broadening (if not due to instrumental artifacts), is under the same restrictions explained by the approximate lattice factor G.

In the SPA-LEED system, as explained in Sec. 3.7, the geometrical angle between the electron gun and channeltron detector is fixed at 4.6°. It should be noted that the angle between the incoming and outgoing beams always remains constant during the variation of the incident angle using electrostatic deflection plates. A schematic diagram of SPA-LEED optics is shown in Fig. 4.6 and the Ewald sphere construction for SPA-LEED differs from that for the conventional LEED. Since the angle between $\boldsymbol{k}_i$ and $\boldsymbol{k}_f$ remains constant during scanning of the deflection voltage, the absolute value of the $\boldsymbol{k}$ remains constant and only its orientation with respect to the surface varies. Hence, in the modified Ewald construction for SPA-LEED, the $\boldsymbol{k}$ is used as the radius of the Ewald sphere instead of the $\boldsymbol{k}_i$ in the conventional Ewald construction (Fig. 4.7). Because of the doubled radius in the modified Ewald sphere, the scanning range in the reciprocal space is doubled in SPA-LEED for a given energy as compared with the conventional LEED.

4.3 Temperature programed desorption[12-17]

One of the simplest qualitative or quantitative experiments that may be carried out on a surface containing an adsorbed layer involves the thermal desorption of species from the surface. An adsorbed species, bound to the surface via van der Waals forces (physisorption) or by chemical bonding (chemisorption), resides on the surface in its adsorption potential well. At a characteristic temperature it starts to desorb from the surface via an activated process. Knowledge of the nature of the desorption process has fundamental implications to understanding the nature of the elementary chemical process in the layer, to the energetics of bonding and the specification of the chemical of the bound species, and to the nature and magnitude of interaction effects between adsorbate species. For example, the kinetic order of a desorption process may suggest the nature of the elementary step(s) governing the process. Zero-order kinetics is often indicative of desorption from a multilayer where the rate of desorption is independent of surface coverage. Zero-order kinetics may also be evidence of equilibrium between different surface phases, with one phase maintaining a constant surface concentration of the desorbing phase. First-order kinetics may be indicative of the presence of a single surface species, while second-order kinetics is an indication of the adsorbate atom recombination process leading to the production of a diatomic molecule that is then evolved.

In TPD, a temperature ramp is applied to the sample and the rate of desorption is followed by monitoring the amount of adsorbate desorbed into the gas phase as a function of temperature. As the temperature rises and the thermal energy available becomes sufficient to break the surface bonds, desorption is observed. For the simple case of an adsorbate in which the activation energy for desorption is constant as a function of coverage, a single desorption peak is obtained. Furthermore, as the experiment is performed in a vacuum chamber that is being continually pumped, the temperature at which maximum desorption occurs, corresponds to the maximum desorption rate. At first sight this may seem unusual since desorption is an activated process with a rate constant k_d that obeys an Arrhenius dependency and hence should increase exponentially with temperature

$$k_d = \nu_d \exp\left(\frac{-E_d}{RT}\right) \tag{4.15}$$

where E_d is the activation energy for desorption and ν_d is a pre-exponential factor. A maximum is observed, because k_d increases exponentially with temperature, and the surface coverage decreases simultaneously as illustrated in Fig. 4.8 for first-order desorption. The observed desorption kinetics are therefore a convolution of these two factors (Polanyi-Wigner equation)

$$r(\theta,T) = -\frac{d\theta}{dt} = \nu_d(\theta,T)\theta^{n(\theta)}\exp\left[\frac{-E_d(\theta)}{RT}\right] \tag{4.16}$$

where r is the rate of desorption, θ is the surface coverage, t is the time, and n is the desorption order.

In equation (4.15), we assumed E_d and ν_d to be independent of coverage. However, all three kinetic parameters, n, E_d, and ν_d, may be coverage dependent and at least ν_d may depend upon temperature. One of the goals of TPD studies is to determine these three kinetic parameters. Several procedures exist for the evaluation of these quantities. The procedures may be divided into two categories: (1) the integral approach[12-15] which relates the kinetic parameters to whole peak characteristics, such as half-widths and temperatures at peak maxima. It is well known that this strategy is useful only in cases where the parameters are not coverage dependent; (2) differential analysis,[16,17] where desorption rate/temperature pairs taken from one or more TPD spectra are used to prepare an Arrhenius plot whose slope and intercept are related to E_d, and ν_d. While integral techniques may be used to extract the coverage-independent kinetic parameters, differential techniques can, in favorable situations, be applied to obtain reliable coverage-dependent kinetic parameters.

Figures

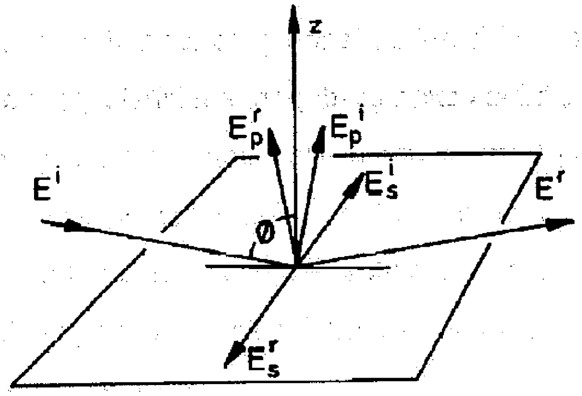

Fig. 4. 1. The reflection geometry showing the *S* and *P* components of the electric fields of incident (E^i) and reflected (E^r) radiation.[1]

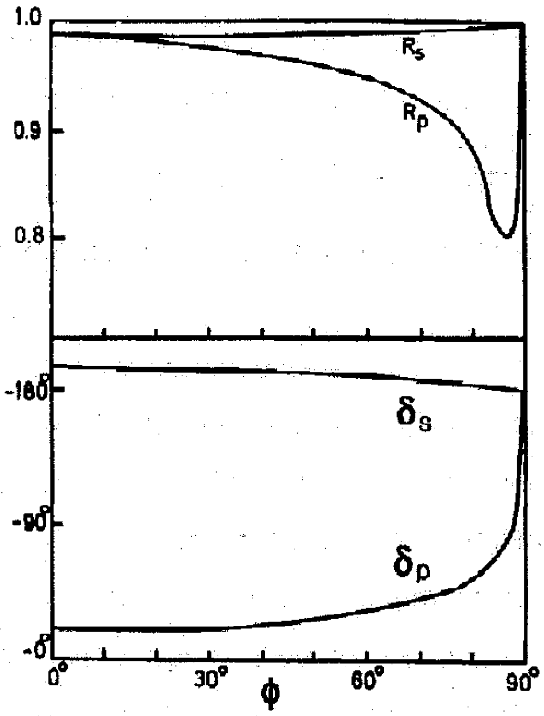

Fig. 4. 2. The intensity coefficients (R) and phase shift (δ) of the *S* and *P* components of the infrared radiation on reflection from a metal (n = 3, k = 30) surface.[1]

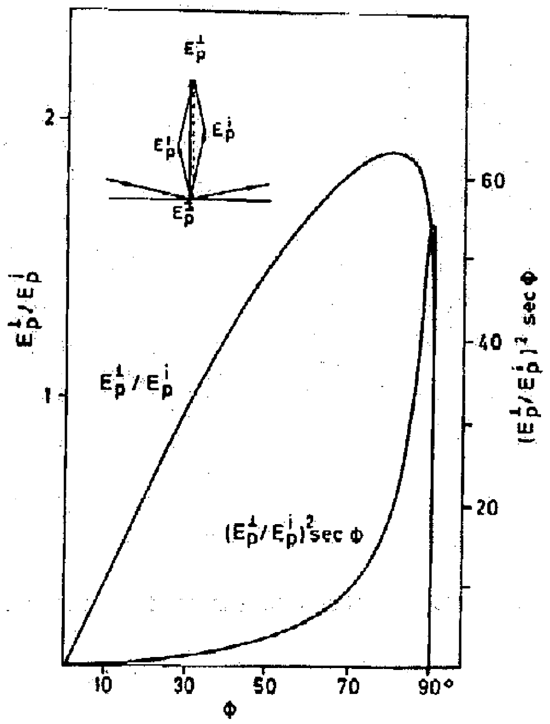

Fig. 4. 3. The relative amplitude $\left(E_p^{\perp}/E_p^{i}\right)^2$ of the electric field perpendicular to the surface as a function of incident angle ϕ, together with the quality $\left(E_p^{\perp}/E_p^{i}\right)^2 \sec\phi$.[1]

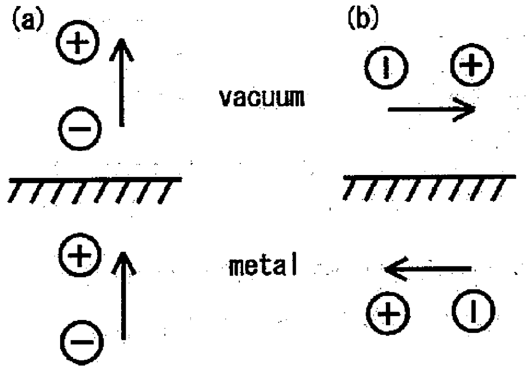

Fig. 4. 4. The image dipole picture of the metal's screening of a dipole oriented (a) perpendicular and (b) parallel to the surface.[1]

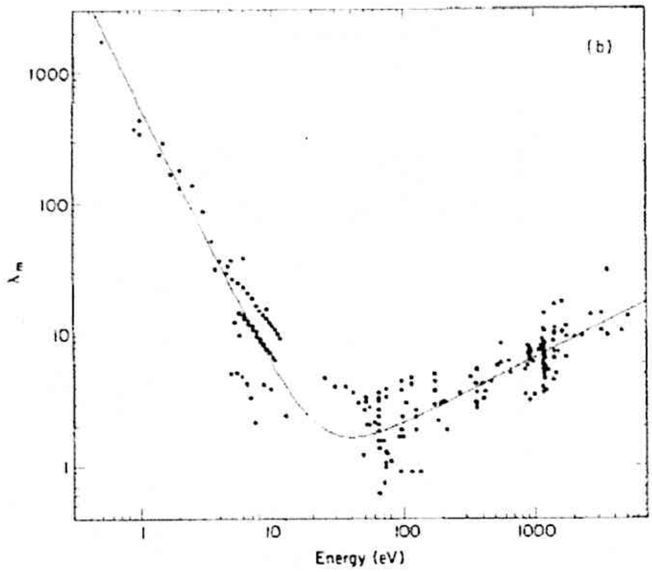

Fig. 4. 5. Mean free path (monolayers) of electrons in solids as a function of their energy.[6]

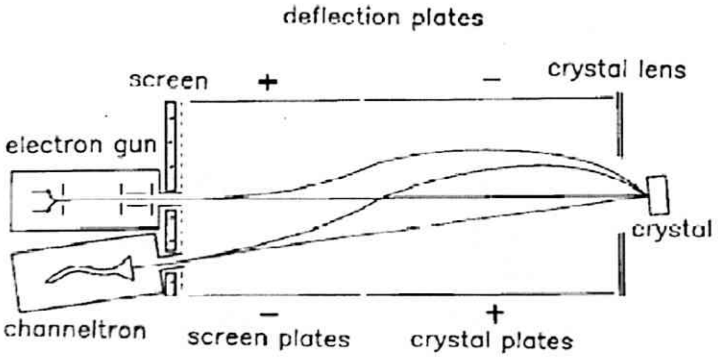

Fig. 4. 6. Electrostatic deflection of the SPA-LEED system with and without deflection voltages. Applying voltages at the plates, both the incoming and outgoing beams are deflected simultaneously in the same way.[11]

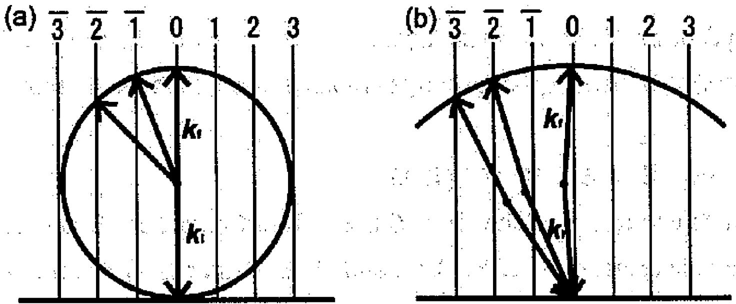

Fig. 4. 7. (a) Ewald construction for conventional LEED system. (b) Modfied Ewald construction for SPA-LEED system. The sphere has a radius of $|k_f - k_i|$, which is almost two (2cos4.6°) times larger than the $|k_i|$.

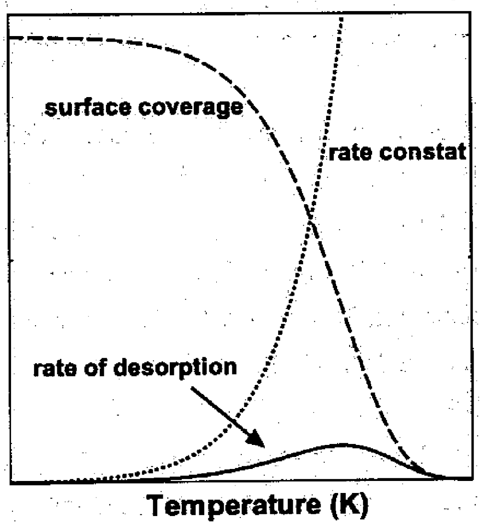

Fig. 4. 8. The rate of desorption (solid line) as a convolution of changes in surface coverage (dashed line) and rate constant (dotted line) as a function of temperature.

References

1. B. E. Hayden, *Ch. 7 Reflection absorption infrared spectroscopy*, in J. T. Yates Jr. and T. E. Madey (ed.) *Vibrational spectroscopy of molecules on surfaces* (Plenum Press, New York, 1987).
2. H. Ueba, Prog. Surf. Sci. **22**, 181 (1986).
3. A. M. Bradshaw and E. Schweizer, *Ch. 8 Infrared reflection-absorption spectroscopy of adsorbed molecules*, in R. J. H. Clark and R. E. Hester (ed.) *Advances in Spectroscopy: Spectroscopy of Surfaces* (Willey, New York, 1988).
4. Y. J. Chabal, Surf. Sci. Rep. **8**. 211 (1988).
5. R. Ryberg, *Infrared Spectroscopy of molecules adsorbed on metal surfaces* p.1-, in K. P. Lawley (ed.) *Advances in Chemical Physics: Molecule surface interactions* (Willey, New York, 1989).
6. M. A. Seah and W. A. Dench, Surf. Interf. Anal, **1**, 2 (1979).
7. M. Henzler, *Ch.4 Electron Diffraction and Surface Defect Structure*, in H. Ibach (ed.) *Electron Spectroscopy for Surface Analysis* (Springer, Berlin, Heidelberg 1977).
8. M. Henzler, Appl. Surf. Sci. **11/12**, 450 (1982).
9. G. Ertl and J. Kuppers, *Ch. 9 Low energy electron diffraction*, in G. Giesler and C. D. –Brenzinger (ed.) *Low Energy Electrons and Surface Chemistry* (Verlag Chemie, Weinheim, 1985).
10. M. A. Van Hove, W. H. Weinberg, and C. –M. Chan, *Low-Energy Electron Diffraction* (Springer, Berlin, Heidelberg 1986).
11. M. Henzler, Surf. Sci. **178**, 441 (1986).
12. J. T. Yates, *Ch.8 The thermal desorption of adsorbed species*, in R. L.Park and M. G. Lagally (ed.) *Methods of Experimental Physics*, Vol. 22 (Academic, New York, 1985).
13. P. A. Redhead, Vacuum. **12**, 203 (1962).
14. D. Edwards, Jr., Surf. Sci. **54**, 1 (1976).
15. C. –M. Chan, R. Aris, and W. H. Weinberg, Appl. Surf. Sci. **1**, 360 (1978).
16. E. Habenschaden and J. Küppers, Surf. Sci. **138**, L147 (1984).
17. J. B. Miller, H. R. Siddiqui, S. M. Gates, J. N. Russel, Jr., J. T. Yates, Jr., J. C. Tully, and M. J. Cardillo, J. Chem. Phys. **87**, 6725 (1987).

Chapter 5

Transient diffusion and cluster formation of water molecules on Rh(111) at 20 K

The initial stage of water adsorption on Rh(111) at 20 K was investigated, using infrared reflection absorption spectroscopy. In this low coverage region, isolated water molecules and small water clusters are observed. Since thermal diffusion is suppressed at 20 K, the formation of water clusters at low coverage is controlled by both coverage and transient diffusion on the surface. Within a simple isotropic diffusion model as the transient diffusion and clustering process, we estimate the mean lateral displacement from the first impact point to the final adsorption site to be 7.6 Å; an incoming water molecule on Rh(111) is trapped with eight post-collision hops on average.

5.1 Introduction

In this chapter, the transient diffusion and the cluster formation of water molecules on Rh(111) upon chemisorption at 20 K is investigated. When a gaseous molecule adsorbs on a surface, adsorption energy is dissipated to the heat bath of a substrate via electron-hole pair (EHP) and phonon excitations.[1] In this process, adsorption energy is partly transferred to kinetic energy, inducing the nonthermal motion of an incoming molecule on the surface. The surface diffusion in such thermalization process is called transient diffusion and this process is important for an essential understanding of energy dissipation during the adsorption and clustering process. Over the past decade, there have been several experimental reports on transient diffusion on surfaces[1-4].

In the case of physisorption, energy dissipation via EHP excitations tends to be inefficient,[1] while the diffusion barrier is also usually very small,[5] meaning that its transient diffusion ranges over hundreds of Å. For example, the mean free path of an incoming O_2 on Ag(110) was in the order of 100 Å[2] and a Xe atom transiently traveled hundreds of angstroms on Pt(111) upon adsorption[3]. On the other hand, as a typical example of chemisorption, Yoshinobu *et al.* experimentally estimated the mean lateral displacement from the first impact point to the final adsorption (chemisorption) site to be 6.8 Å for CO on the Pt(111) terrace,[4] where the coupling to EHP excitations causes a significant quenching of transient diffusion.[6] How about weak chemisorption systems, such as water adsorption on transition metal surfaces? Recently, Kimmel *et al.* reported the importance of the transient diffusion of water molecules in thin film growth on Pt(111), where the amorphous water film shows layer-by-layer growth for at least first three layers by transient diffusion.[7] In order to explain the layer-by-layer growth, they estimated the number of transient diffusion steps using a random walk model with a simple cubic lattice to be ~10 steps,[7] which means a lower limit of the transient diffusion steps in the model. Yamamoto *et al.* reported that smaller two dimensional (2D) islands are formed on Rh(111) compared with the case on Pt(111) and Ni(111) at low temperature; the transient diffusion of water molecules is relatively limited on the Rh(111) surface.[8] Therefore, the transient diffusion of water molecules on transition metal surfaces plays an important role in adsorption, clustering, and island growth at low temperature. In this study, I estimated lateral displacement of an incoming water molecule on the Rh(111) surface experimentally.

I investigated the initial stage of water adsorption on Rh(111) at 20 K using infrared reflection absorption spectroscopy (IRAS). Since thermal diffusion was suppressed at 20 K,[8] the formation of water clusters at low coverage should be controlled by both the coverage and transient diffusion on the surface, as illustrated in Fig. 5.1. With increasing coverage, the collision (cluster formation) probability of a transiently diffusing water molecule with a pre-adsorbed monomer increases, so the number of monomers eventually decreases. Therefore, the use of a certain model concerning transient diffusion allows the transient diffusion length to be estimated by comparing the simulated transient diffusion and clustering process with the experimental results.

5.2 Experimental

The experimental conditions and sample preparation were described in section 3.3 and water coverage was estimated via temperature programmed desorption (see chapter 6).[9] In this section, I assume that the coverage of water monolayer corresponds to 0.67 ML [= 1 BL (bilayer): 1.07×10^{15} molecules/cm^2]. IRAS measurements were performed using an FTIR spectrometer (Bruker IFS66v/S) with a mercury–cadmium–telluride (MCT; HgCdTe) detector. All the spectra were measured with a sample temperature of 20 K with 4 cm^{-1} resolution and 500 scans. Water molecules were adsorbed at 20 K.

5.3 Results and Discussion

Figure 5.2 shows a series of IRAS spectra of the HOH bending (δ_{HOH}) mode region as a function of H_2O coverage at 20 K. At the initial stage of H_2O adsorption, a sharp peak is observed at 1569 cm^{-1}. This peak subsequently increases in intensity and new peaks appear at 1587 and 1608 cm^{-1} with increasing coverage. According to our previous report about D_2O/Rh(111),[8] these peaks at 1569, 1587 and 1608 cm^{-1} can be assigned to the δ_{HOH} mode of monomer, dimer and larger clusters, respectively. Note that, in this study, I focus on the δ_{HOH} mode, because the absorbance of the OH stretching (ν_{OH}) mode is much weaker in the case of monomer and small water clusters than that of the δ_{HOH} mode.[8]

Since no time-evolution was observed in IRAS spectra at 20 K, I conclude that thermal diffusion is suppressed and the clustering of water molecules is controlled by transient diffusion upon adsorption at the present condition, meaning that the number of monomers depends on the transient diffusion length as a function of coverage. Note that vibrational peaks do not shift with increasing coverage (Fig. 5.2), which indicates that the adsorbed water species (monomer and clusters) do not interact with each other; they are isolated water species.

Figure 5.3(a) shows the integrated absorbance of δ_{HOH} modes (1569, 1587 and 1608 cm^{-1}) as a function of total H_2O coverage. For the monomeric δ_{HOH} mode (1569 cm^{-1}), the intensity grows almost linearly up to θ=0.01 ML, meaning the monomer is the predominant species in this coverage region. The rate of growth, however, decreases at θ~0.02 ML, which indicates that water clusters start forming and the intensity remains nearly constant at $\theta \geq 0.04$ ML. This coverage dependence results from the cluster formation, which is controlled by transient diffusion. Therefore, the transient diffusion length could be estimated by comparing the simulated coverage dependence of monomer species, based on a certain model, with the experimental results.

I have simulated the transient diffusion and clustering process based on the following stochastic model. (1) A simple isotropic diffusion model was used as the transient diffusion. When a water molecule adsorbs on the surface from the gas phase, it randomly collides with the surface and migrates with an *N*-step isotropic diffusion from the collision point. One step corresponds to a lateral hop from an atop site to one adjacent on Rh(111). In this simulation, the only parameter is the number of steps, *N*. (2) Once a mobile water molecule encounters a pre-adsorbed molecule at one of its nearest neighbor sites within *N* steps, the water molecule always forms a cluster (dimer, trimer, etc.) with a pre-adsorbed water, irrespective of the molecular orientation. This assumption may be reasonable in the case of dimer formation, since a water monomer may be rotating on the surface at temperatures above a few K.[10,11] Note that diffusion via other sites (bridge, hollow, etc) might lead to the formation of clusters in the real system, but I used site-to-site hopping between atop sites. (3) When an incoming molecule impinges upon a pre-adsorbed molecule, it randomly adsorbs at one of the six nearest neighbor sites to form two-dimensional clusters (i.e. molecules do not form clusters normal to the surface). (4) The (111) surface with 30 x 30 on-top sites and periodic boundary conditions were used. Note that the present model does not require any parameters for kinetics and energetics.

Figure 5.3(b) shows a snap shot for $N = 8$ at 0.04 ML; there are monomers, dimers, trimer, and tetramer. In the model, the shape of water clusters is not limited (e.g. three types of trimer species can be formed, such as “line”, “triangle”, and “kinked line”. In Fig. 5.3(b), a trimer species exists as a kinked line). Under these experimental conditions, this simplification makes it less problematic to estimate the transient diffusion length, because monomers and small water clusters are the dominant species (no bilayer island is observed in IRAS).

Based on the model, the number of monomer species was counted as a function of coverage at a certain *N*. Figure 5.3(c) shows the simulated curves for

N = 6, 8, 10, 12, and 14. The simulation is also performed for a simple hit-and-stick model[7] (N = 0), where the vertical growth of molecules on the surface is allowed [Fig. 5.3(c), dashed curve].

All curves exhibit a virtually linear uptake and the same leading edges below θ=0.01 ML, which indicates that monomers are predominant below 0.01 ML. Assuming the integrated absorbance of 1569 cm^{-1} peak [Fig. 5.3(a)] to be proportional to the coverage of monomers, the integrated absorbance of monomers can be converted to the coverage of monomer by fitting the experimental data to the common leading edges in the low coverage region [Fig. 5.3(c)].

By increasing the total coverage, the hit-and-stick model obviously deviates from the observed results. On the other hand, by including the transient diffusion, the gradient of the simulated curves tends to decrease with increasing coverage. In order to obtain the best-fit N, the determination coefficients were calculated as a function of N using the least squares analysis (not shown here). Consequently, the most probable N is determined to be eight. Since the lattice constant of the Rh(111) surface is 2.69 Å, the total path and mean lateral displacement of a water molecule by transient diffusion are estimated at 21.5 Å and 7.6 Å, respectively. In the present isotropic diffusion model, a ballistic transient diffusion (long jump) was not considered, but a similar path length of a mobile monomer should be obtained, irrespective of the models (isotropic diffusion or long jump).

In general, the transient diffusion on surfaces depends on the corrugation of the adsorption potential energy surface (PES) and the dissipation process of the adsorption energy via EHP and phonon excitations. An incoming water molecule to the surface is accelerated by the attractive chemisorption potential and scattered by the corrugated PES at the surface; its kinetic energy is 0.43~0.47 eV (an adsorption energy of 0.38~0.42 eV[10-12] plus the kinetic energy of the incoming molecule of $2k_BT$~0.05 eV at 300 K) in the near vicinity of the surface prior to a scattering event. This results in various excitations, including the rotation, vibration, and translation of the molecule. The relaxation of the ν_{OH} or the δ_{HOH} energy could induce lateral hopping by an anharmonic coupling to low energy hindered rotations/translations.[13,14] Here, the vibrational energies of the ν_{OH} and the δ_{HOH} modes on Pt(111) are calculated at 0.44 eV and 0.19 eV, respectively,[10] and the excitation energy for H_2O on Rh(111) may be similar. The excitation energy of the ν_{OH} mode (0.44 eV) is comparable with the kinetic energy (0.43~0.47 eV). Thus, the ν_{OH} mode of the incoming H_2O molecule could be excited in the adsorption process. On the other hand, the vibrational energies of the ν_{OD} and δ_{DOD} modes of D_2O/Pt(111) are 0.33 and 0.14 eV, respectively.[10] These energies are lower than the kinetic energy of the incoming water molecule (0.43~0.47 eV), meaning a different transient diffusion process might occur in the cases of H_2O and D_2O. However, no isotope effect was observed within the present experiments.

The shape of PES is characterized by a corrugation ratio (E_{diff}/E_{des}), where E_{diff} and E_{des} are activation energies for diffusion and desorption, respectively[1]. If the corrugation ratio is small (large), an incoming water molecule feels a smooth (rough) PES. The larger a corrugation ratio, the more effectively the surface would trap an incoming molecule. For H_2O/Pd(111), E_{diff} and E_{des} were calculated to be 0.20 eV and 0.33 eV[15], respectively, with a corrugation ratio of 0.60. In addition, based on theoretical calculations for H_2O/Al(100) and D_2O/Ru(0001), the corrugation ratios are 0.17/0.34 = 0.50[16] and 0.31/0.41 = 0.76[17], respectively, which are relatively high compared with other chemisorption systems on transition metal surfaces (table 5.1).[5] According to these reports,[15-17] I also expect the corrugation ratio for water on Rh(111) to be significant. Therefore, when a water molecule enters such a PES, it could be trapped (chemisorbed) in one of the PES minima on the transition metal surfaces within several post-collision hops.

5.4 Conclusion

In summary, I investigated the initial stage of water adsorption on Rh(111) at 20 K by IRAS. The transient diffusion length was estimated by counting the number of water monomers as a function of total coverage. Using the simulation based on the isotropic diffusion model, the total length and mean lateral displacement by the transient diffusion of a water molecule on Rh(111) were estimated at 21.5 Å and 7.6 Å, respectively.

Figures

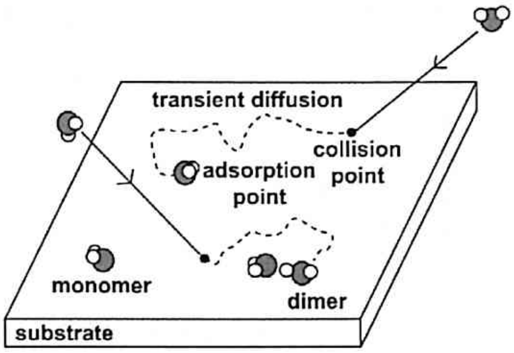

Fig. 5. 1. A schematic model of transient diffusion and clustering of water molecules. Gaseous molecules randomly collide with the surface, and then transiently diffuse on the surface. If a water molecule encounters other molecules during transient diffusion, a water cluster (i.e. dimer) is formed.

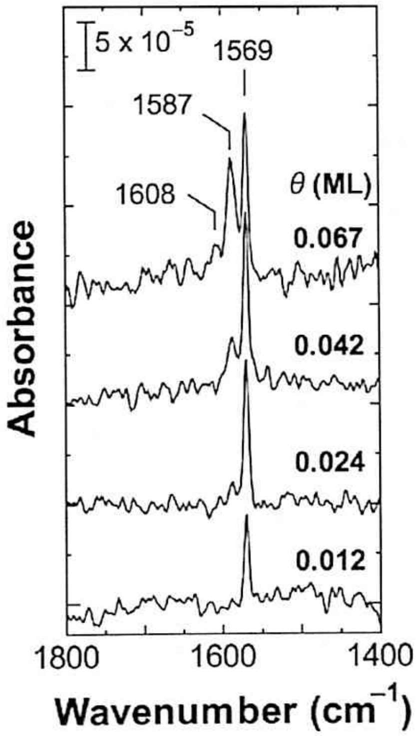

Fig. 5. 2. IRAS spectra of the δ_{HOH} mode for H_2O on Rh(111) as a function of coverage. Water molecules were adsorbed at 20 K. All the spectra were measured at 20 K and 4 cm^{-1} resolution.

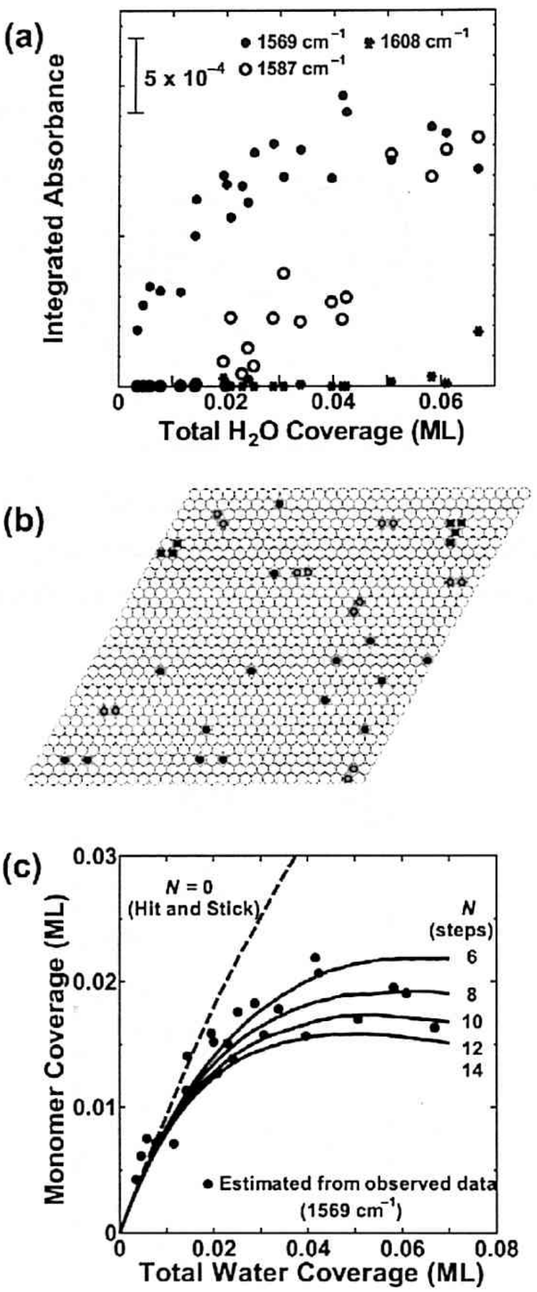

Fig. 5. 3. (a) Integrated absorbance of the peaks observed at 1569, 1587 and 1608 cm^{-1} as a function of coverage. (b) A simulated result for $N = 8$ at 0.04 ML. The monomer, dimer, and larger clusters are represented as a filled circle, gray circle, and filled square, respectively. (c) Simulated curves of the coverage of monomer species as a function of total water coverage with (solid curves) and without (hit-and-stick model, dashed curve) transient diffusion. Estimated coverages of monomer species from the observed data are plotted as a filled circle.

Adsorption system	E_{diff} (eV)	E_{des} (eV)	E_{diff} / E_{des}	Mean lateral displacement (Å)
CO/Pt(997)*	0.19**5)	~1.3**5)	~0.15	6.84)
NO/Pt(997)*	0.2918)	~2.0 (theory)18)	0.15	4.118)
H_2O/Rh(111)	—	0.38 (theory)12)	—	7.6

Table 5. 1. Previous and present results of transient diffusion length for chemisorption system. *The Pt(997) surface has a periodic step-terrace structure. The terrace of this surface has a (111) close-packed structure, constituted by nine rows of Pt atoms, and the monatomic step is formed by a (111) microfacet. **Reported value for the Pt(111) terrace.

References

1. J. V. Barth, Surf. Sci. Rep. **40**, 75 (2000).
2. J. V. Barth, T. Zambelli, J. Wintterlin, and G. Ertl, Chem. Phys. Lett. **270**, 152 (1997).
3. P. S. Weiss and D. M. Eigler, Phys. Rev. Lett. **69**, 2240 (1992).
4. J. Yoshinobu, N. Tsukahara, F. Yasui, K. Mukai, and Y. Yamashita, Phys. Rev. Lett. **90**, 248301 (2003).
5. E. G. Seebauer and C. E. Allen, Prog. Surf. Sci. **49**, 265 (1995).
6. J. T. Kindt, J. C. Tully, M. H-Gordon, and M. A. Gomez, J. Chem. Phys. **109**, 3629 (1998).
7. G. A. Kimmel, N. G. Petrik, Z. Dohnálek, and B. D. Kay, J. Chem. Phys. **125**, 044713 (2006).
8. S. Yamamoto, A. Beniya, K. Mukai, Y. Yamashita, and J. Yoshinobu, J. Phys. Chem. B. **109**, 5816 (2005).
9. A. Beniya, S. Yamamoto, K. Mukai, Y. Yamashita, and J. Yoshinobu, J. Chem. Phys. **125**, 054717 (2006).
10. S. Meng, E. G. Wang, and S. Gao, Phys. Rev. B. **69**, 195404 (2004).
11. A. Michaelides, V. A. Ranea, P. L. de Andres, and D. A. King, Phy. Rev. Lett. **90**, 216102 (2003).
12. P. Vassilev, R. A. van Santen, and M. T. M. Koper, J. Chem. Phys. **122**, 054701 (2005).
13. E. Fomin, M. Tatarkhanov, T. Mitsui, M. Rose, D. F. Ogletree, and M. Salmeron, Surf. Sci. **600**, 542 (2006).
14. K. Morgenstern and K-H. Rieder, J. Chem. Phys. **116**, 5746 (2002).
15. V. A. Ranea, A. Michaelides, R. Ramírez, P. L. de Andres, J. A. Vergés, and D. A. King, Phys. Rev. Lett. **92**, 136104 (2004).
16. J. Li, Y. Li, S. Zhu, and F. Wang, Phys. Rev. B. **74**, 153415 (2006).
17. S. Meng, E, G. Wang, Ch. Frischkorn, M. Wolf and S. Gao, Chem. Phys. Lett. **402**, 384 (2005).
18. N. Tsukahara, K. Mukai, Y. Yamashita, and J. Yoshinobu, J. Chem. Phys. (in press).

Appendix

The source code of the present isotropic diffusion and clustering simulation

In this study, I created a simulation program based on the stochastic diffusion model with Gourmet in order to estimate the transient diffusion length of water molecules on the Rh(111) surface.

Gourmet is performed using Python programming language. In this section, the source code of the program is shown. [Reference: M. Doi and J. Takimoto, buturikasouzikkensitu (nagoyadaigakushuppankai, 2004), in Japanese]

Input the cell size, coverage, the number of diffusion steps, and of trial runs.

```
¥begin{global_def}
class Vector2d: {x: int, y: int}

input: {
        cell: int "size of unit cell"
        coverage: double "ML"
        N: int "number of diffusion steps"
        P: int "number of trial run"
}

output_summary:{
        average[]:{
                ave_coverage: double
                ave_monomer: double
                ave_dimer: double
                ave_larger_cluster: double
        }
}
```

```
¥end{global_def}

¥begin{def}
output: {
        statistics[]: {
                molecule[]: {
                        site: Vector2d
                        nearest_site[]: Vector2d
                }
                count[]:{
                        coverage: double
                        monomer: int
                        dimer: int
                        larger_cluster: int
                }
        }

}
¥end{def}

¥begin{data}
input: {30, 0.07, 8, 1000}
¥end{data}
```

Phyton program for the isotropic diffusion-clustering simulation.

```
# definition of the six nearest neighbor sites
def nearest(n,m,i,s):
        # first site
        n_near1 = n + 1
        m_near1 = m
        if n_near1 == n0:
                n_near1 = 0
        $output.statistics[s].molecule[i].nearest_site[0] = [n_near1,m_near1]
        # second site
```

```
    n_near2 = n
    m_near2 = m + 1
    if m_near2 == m0:
        m_near2 = 0
    $output.statistics[s].molecule[i].nearest_site[1] = [n_near2,m_near2]
    # third site
    n_near3 = n - 1
    m_near3 = m + 1
    if n_near3 == -1:
        n_near3 = n0 - 1
    if m_near3 == m0:
        m_near3 = 0
    $output.statistics[s].molecule[i].nearest_site[2] = [n_near3,m_near3]
    # fourth site
    n_near4 = n - 1

    m_near4 = m
    if n_near4 == -1:
        n_near4 = n0 - 1
    $output.statistics[s].molecule[i].nearest_site[3] = [n_near4,m_near4]
    # fifth site
    n_near5 = n
    m_near5 = m - 1
    if m_near5 == -1:
        m_near5 = m0 - 1
    $output.statistics[s].molecule[i].nearest_site[4] = [n_near5,m_near5]
    # sixth site
    n_near6 = n + 1
    m_near6 = m -1
    if n_near6 == n0:
        n_near6 = 0
    if m_near6 == -1:
        m_near6 = m0 -1
    $output.statistics[s].molecule[i].nearest_site[5] = [n_near6,m_near6]

# definition of the method to count the number of monomer species
```

```
def monomer_count(i,s):
          monomer = 0
          for k in range(0,i+1):
                    for l in range(0,i+1):
                              if $output.statistics[s].molecule[l].site in
$output.statistics[s].molecule[k].nearest_site[]:
                                        break
                              elif l == i:
                                        monomer = monomer + 1
          $output.statistics[s].count[i].monomer = monomer

# definition of the method to count the number of dimer species
def dimer_count(i,s):
          dimer = 0
          for x in range(0,i+1):
                    for y in range(0,i+1):
                              if $output.statistics[s].molecule[y].site in
$output.statistics[s].molecule[x].nearest_site[]:
                                        if i == 1:
                                                  dimer = dimer + 1
                                        else:
                                                  z = range(i+1)
                                                  if x < y:
                                                            del z[y]
                                                            del z[x]
                                                  elif x > y:
                                                            del z[x]
                                                            del z[y]
                                                  for v in z:
                                                            if $output.statistics[s].molecule[v].site
in $output.statistics[s].molecule[x].nearest_site[]:
                                                                      break
                                                            elif $output.statistics[s].molecule[v].site
in $output.statistics[s].molecule[y].nearest_site[]:
                                                                      break
                                                            elif v == z[i-2]:
```

```
                            dimer = dimer + 1
                    break
    $output.statistics[s].count[i].dimer = dimer

# definition of the method to count the number of larger clusters
def count(i,s):
    monomer_count(i,s)
    dimer_count(i,s)
    larger =
i+1-(($output.statistics[s].count[i].monomer)+($output.statistics[s].count[i].dimer))
    $output.statistics[s].count[i].coverage = (i+1)*1.00000/($input.cell)**2
    $output.statistics[s].count[i].larger_cluster = larger

from math import *
from Numeric import *
from RandomArray import *
n0 = $input.cell
m0 = $input.cell
imax = int($input.coverage*(n0**2))

smax = $input.P
for s in range(0,smax):
# randomly locate the first molecule (i=0)
    i = 0
    d1 = uniform(0,n0,[imax,2])
    n1 = int(d1[0][0])
    m1 = int(d1[0][1])

    $output.statistics[s].molecule[0].site = [n1, m1]
    nearest(n1,m1,i,s)
    $output.statistics[s].count[0] = [1.00000/($input.cell)**2,1,0,0]
# randomly locate the next molecule (i≧1), and then isotropically diffuse
    sites = []
    nearest_sites = []
    for i in range(1,imax):
        n = int(d1[i][0])
```

```
        m = int(d1[i][1])
        i2 = 0
        i2max = $input.N   # i2 = step number
        sites.append([$output.statistics[s].molecule[i-1].site])
        for i7 in range(0,6):

    nearest_sites.append([$output.statistics[s].molecule[i-1].nearest_site[i7]])

        while i2 < i2max:
# if the diffusing molecule comes at one of the nearest neighbor sites of pre-adsorbed molecules
            if [[n,m]] in nearest_sites and not [[n,m]] in sites:
                $output.statistics[s].molecule[i].site = [n,m]
                nearest(n,m,i,s)
                count(i,s)
                break
# isotropic diffusion
            else:
                i2 = i2+1
                p = uniform(0,1,[1,1])
                if 0<=p<1.0/6:
                    n = n + 1
                elif 1.0/6<=p<2.0/6:
                    m = m + 1
                elif 2.0/6<=p<3.0/6:
                    n = n - 1
                    m = m + 1
                elif 3.0/6<=p<4.0/6:
                    n = n - 1
                elif 4.0/6<=p<5.0/6:
                    m = m - 1
                else:
                    n = n + 1
                    m = m - 1
# periodic boundary
                if n == n0:
                    n = 0
```

```
                if m == m0:
                    m = 0
                if n == -1:
                    n = n0 -1
                if m == -1:
                    m = m0 -1
                if i2 == i2max and [[n,m]] in nearest_sites:
                    $output.statistics[s].molecule[i].site = [n,m]
                    nearest(n,m,i,s)
                    count(i,s)
                elif i2 == i2max:
                    $output.statistics[s].molecule[i].site = [n,m]
                    nearest(n,m,i,s)
                    count(i,s)

# output the coverage, the number of monomer, dimer, and larger clusters
for q in range(0,imax):
    cov = $output.statistics[0].count[q].coverage
    mono = 0.00
    di = 0.00
    larg = 0.00
    for w in range(0,smax):
        mono = mono + $output.statistics[w].count[q].monomer
        di = di + $output.statistics[w].count[q].dimer
        larg = larg + $output.statistics[w].count[q].larger_cluster
    $output_summary.average[q]                                            =
[cov,mono*1.0000/smax,di*1.0000/smax,larg*1.0000/smax]
```